The miniJPAS survey : Galaxy populations in the most massive cluster in miniJPAS: mJPC2470-1771

Rodriguez-Martin, J. E.

2022-10-21

http://hdl.handle.net/10138/352850
https://doi.org/10.1051/0004-6361/202243245

Astronomy & Astrophysics

The miniJPAS survey

Galaxy populations in the most massive cluster in miniJPAS: mJPC2470-1771

J. E. Rodríguez-Martín[1] , R. M. González Delgado[1], G. Martínez-Solaeche[1], L. A. Díaz-García[1], A. de Amorim[2],
R. García-Benito[1], E. Pérez[1], R. Cid Fernandes[2], E. R. Carrasco[3], M. Maturi[4,5], A. Finoguenov[6], P. A. A. Lopes[7],
A. Cortesi[7], G. Lucatelli[8], J. M. Diego[9], A. L. Chies-Santos[10,11], R. A. Dupke[12,13,14], Y. Jiménez-Teja[1],
J. M. Vílchez[1], L. R. Abramo[15], J. Alcaniz[10,12], N. Benítez[1], S. Bonoli[16,17,19], A. J. Cenarro[17,18],
D. Cristóbal-Hornillos[17], A. Ederoclite[21], A. Hernán-Caballero[17], C. López-Sanjuan[17,18], A. Marín-Franch[17,18],
C. Mendes de Oliveira[21], M. Moles[1,17], L. Sodré Jr.[21], K. Taylor[21], J. Varela[17,18],
H. Vázquez Ramió[17,18], and I. Márquez[1,20]

(Affiliations can be found after the references)

Received 1 February 2022 / Accepted 20 July 2022

ABSTRACT

The Javalambre-Physics of the Accelerating Universe Astrophysical Survey (J-PAS) is a photometric survey that is poised to scan several thousands of square degrees of the sky. It will use 54 narrow-band filters, combining the benefits of low-resolution spectra and photometry. Its offshoot, miniJPAS, is a 1 $\deg^2$ survey that uses J-PAS filter system with the Pathfinder camera. In this work, we study mJPC2470-1771, the most massive cluster detected in miniJPAS. We survey the stellar population properties of the members, their star formation rates (SFR), star formation histories (SFH), the emission line galaxy (ELG) population, spatial distribution of these properties, and the ensuing effects of the environment. This work shows the power of J-PAS to study the role of environment in galaxy evolution. We used a spectral energy distribution (SED) fitting code to derive the stellar population properties of the galaxy members: stellar mass, extinction, metallicity, $(u-r)_{res}$ and $(u-r)_{int}$ colours, mass-weighted age, the SFH that is parametrised by a delayed-τ model (τ, t_0), and SFRs. We used artificial neural networks for the identification of the ELG population via the detection of the Hα, [NII], Hβ, and [OIII] nebular emission. We used the Ew(Hα)-[NII] (WHAN) and [OIII]/Hα-[NII]/Hα (BPT) diagrams to separate them into individual star-forming galaxies and AGNs. We find that the fraction of red galaxies increases with the cluster-centric radius; and at $0.5R_{200}$ the red and blue fractions are both equal. The redder, more metallic, and more massive galaxies tend to be inside the central part of the cluster, whereas blue, less metallic, and less massive galaxies are mainly located outside of the inner $0.5R_{200}$. We selected 49 ELG, with 65.3% of them likely to be star-forming galaxies, dominated by blue galaxies, and 24% likely to have an AGN (Seyfert or LINER galaxies). The rest are difficult to classify and are most likely composite galaxies. These latter galaxies are red, and their abundance decreases with the cluster-centric radius; in contrast, the fraction of star-forming galaxies increases outwards up to R_{200}. Our results are compatible with an scenario in which galaxy members were formed roughly at the same epoch, but blue galaxies have had more recent star formation episodes, and they are quenching out from within the cluster centre. The spatial distribution of red galaxies and their properties suggest that they were quenched prior to the cluster accretion or an earlier cluster accretion epoch. AGN feedback or mass might also stand as an obstacle in the quenching of these galaxies.

Key words. galaxies: clusters: individual: mJPC2470-1771 – galaxies: evolution – galaxies: photometry – galaxies: stellar content – galaxies: star formation

1. Introduction

Galaxies in clusters interact with each other as well as with the intracluster medium through processes such as ram-pressure stripping (Gunn et al. 1972), tidal stripping (Malumuth & Richstone 1984), or harassment (Moore et al. 1996). These processes affect the galaxies' star formation and evolutionary processes and can lead to a greater presence of massive galaxies in dense environments and lower star formation rates (SFRs) in such regions (e.g., Lewis et al. 2002; Gómez et al. 2003; Baldry et al. 2006). Galaxies in clusters are therefore a great laboratory for studying the role of environment in galaxy evolution.

Certainly, interactions within galaxy clusters play a relevant role in the transformation of galaxies (Boselli & Gavazzi 2006). Since the pioneering work by Dressler (1980) it is well-known that there is a morphology-density relation that may imply a connection between dense environments and the transformation and evolution of galaxies. This relation shows that as local galaxy density increases, so does the fraction of early-type galaxies, and the fraction of spirals decreases. Dressler (1980) explains this relation as a reflection of the time scale of the formation of the disc of galaxies. This morphology-density relation has been confirmed by many works both at the levels of the nearby universe (e.g., Cappellari et al. 2011; Fogarty et al. 2014) and at higher redshift (e.g., Muzzin et al. 2012). This relation could be the result of galaxy-galaxy merging processes and ram-pressure stripping, since these activities can lead to the formation of a spheroidal component, resulting in the morphological transformation of late- to early-type galaxies (Boselli et al. 2008; De Rijcke et al. 2010; Joshi et al. 2020; Peschken et al. 2020; Janz et al. 2021).

The effect of dense environments can be also seen in the properties of galaxy populations. Density strongly affects the stellar mass distribution and, at fixed stellar mass, the star formation rate and nuclear activity depend on the density as well,

however, the structural parameters are independent of the environment (Kauffmann et al. 2004). Balogh et al. (2004) showed that, at fixed luminosity, the mean $(u − r)$ colour of red and blue galaxies is almost independent of the environment, but the fraction of red galaxies increases with density. These authors propose that the transformations from blue to red must occur very rapidly (in this case, the process is known as 'quenching') or at high redshift. Along this line, Bower et al. (1990) results also point out that galaxies in denser environments are older on average, meaning that galaxies in denser environments have had their star formation truncated at earlier epochs, as opposed to galaxies in less dense environments. This age-density relation is also seen in red sequence galaxies in the work by Cooper et al. (2010), showing also a weak correlation between metal-rich galaxies and denser environments. This age-density relation is supported by several other works (e.g., Trager et al. 2000; Thomas et al. 2005; Clemens et al. 2006; Bernardi et al. 2006; Smith et al. 2008).

Clusters, in particular those formed at more recent times, are also dynamically in-mature structures that have doubled their mass since $z \sim 0.5$ (Boylan-Kolchin et al. 2009; Gao et al. 2012). The accretion times for $z = 0$ cluster members are quite extended, with ~20% of them incorporated into the cluster halo more than 7 Gyr ago and ~20% within the last 2 Gyr (Berrier et al. 2009). Thus, the galaxy populations in clusters have evolved rapidly since $z \sim 0.5$, with the accretion of star-forming galaxies into the cluster and their transformation into early-type red galaxies.

The so-called Butcher-Oemler effect (Butcher & Oemler 1978, 1984) also reflects the evolutionary nature of clusters. It shows that the fraction of blue galaxies is larger for clusters at higher redshift (e.g., Balogh et al. 2000; Ellingson et al. 2001; Diaferio et al. 2001). Moreover, these studies have found that blue galaxies are mostly located outside the cluster cores and that the effect is not significant for distances larger than $0.5R_{200}$. In fact, passive galaxies are mainly located in the virialised regions while the emission line galaxies are more common in the outskirts of the clusters (Haines et al. 2012, 2015; Noble et al. 2013, 2016; Mercurio et al. 2021). In contrast, the Faint Infrared Grism Survey (FIGS, Pirzkal et al. 2017) revealed that [OIII] emitters are more common close to groups, but there is no evidence of a relation between SFR and local galaxy density (Pharo et al. 2020).

Quenching is an important effect related not only to the environment, but also to the galaxy mass. Peng et al. (2010) separated the effects of the mass and the environment in halting star formation and they considered quenching as a combination of both effects (mass-quenching and environment-quenching). Other works have also shown that certain processes that are in some way related to the galaxy stellar mass can suppress the star formation in galaxies independently of the environment (see e.g., Peng et al. 2012; Arcila-Osejo et al. 2019; Contini et al. 2020; Guo et al. 2021). In fact, AGN feedback can play a relevant role by heating the infalling gas, thus preventing further star formation in the galaxy (Di Matteo et al. 2005; Fabian 2012; McNamara & Nulsen 2012), although this approach remains open for debate (Esposito et al. 2022; Wang & Yang 2022). The central velocity dispersion is correlated with the mass of the central black hole of galaxies, so it is connected the AGN feedback and it has been shown to play a crucial role in quenching (see e.g., Bluck et al. 2020; Brownson et al. 2022).

Some environmental processes can temporarily enhance the star formation due to the inflow of gas toward the central part (e.g., galaxy-galaxy interactions) or the compression of the gas (e.g., ram pressure stripping Joseph & Wright 1985;

Park & Hwang 2009; Ellison et al. 2013; Ruiz-Lara et al. 2020; Boselli et al. 2021; Mazzi et al. 2021; Lizée et al. 2021). Nevertheless, these environment mechanisms eventually shut down the process of star formation by heating or removing the gas from galaxies (Alatalo et al. 2015; Davies et al. 2015; Lisenfeld et al. 2017; Joshi et al. 2019).

Alternatively, the halo mass is proposed as the main property that is causally linked to the rapid shut down of the star formation (see e.g., Bluck et al. 2014; Woo et al. 2015; Montero-Dorta et al. 2021) because the fraction of quenched galaxies is more correlated with the group or cluster halo mass at a fixed $M_\star$ than with $M_\star$ at a fixed halo mass (Woo et al. 2013). A bimodality exists in the specific star formation rates (sSFR, i.e. the ratio of the SFR to the stellar mass) of satellite galaxies (those falling into denser haloes) and they are more likely to be quenched than field galaxies (Wetzel et al. 2012). In addition, mass and environment quenching could be connected to massive halos that heat the cold-accreted gas, thereby preventing further star formation (Dekel & Birnboim 2006). Furthermore, the quenching of satellites is correlated not only to halo-mass, but it is also anticorrelated with regard to the group and cluster radial distance (Woo et al. 2013, 2017). Nonetheless, the IllustrisTNG simulations show that the dependence of the quenched galaxy fraction with the cluster-centric radius is also a function of the mass of halos. Thus, although the fraction of quenched low-mass satellites in less massive halos is higher closer to the centre, it is independent of the distance in massive halos (Donnari et al. 2021). However, after several decades of debate, the relevance of the different processes that can lead to the quenching of star formation and the transformation of galaxies in clusters is not yet clear.

Photometric surveys with broad band filters, such as the Local Cluster Substructure Survey (LoCuSS, Haines et al. 2015), the Advance Large Homogeneous Area Medium Band Redshift Astronomical (ALHAMBRA Ascaso et al. 2015), the VIMOS Public Extragalactic Redshift Survey (VIPERS Haines et al. 2017), the Subaru Strategic Program with the Hyper Suprime-Cam (HSC-SSP, Lin et al. 2017; Jian et al. 2018), and the Gemini Observations of Galaxies in Rich Environments (GOGREEN McNab et al. 2021), have been essential in the detection and study of galaxy clusters. Surveys with narrow band filters at specific wavelengths aimed at selecting emission lines (Lin et al. 2017; Koyama et al. 2018; Hayashi et al. 2020) and identifying infalling galaxies in the outskirt of clusters (Kodama et al. 2004) have been very useful for identifying the galaxy populations in clusters. However, these surveys could suffer from several problems related to contamination from: 1) field interlopers due to the lack of precise redshifts for the galaxy cluster membership; 2) dusty star-forming galaxies in the cluster red galaxy population due to the non-correction of colours by extinction; 3) AGNs in the star-forming galaxy population. Furthermore, the small FoV of some instruments, (e.g., with Tunable Filters, as in Sánchez-Portal et al. 2015; Rodríguez del Pino et al. 2017) hinders the observation of the whole cluster or beyond the cluster centre.

The Javalambre-Physics of the Accelerating Universe Astrophysical Survey (J-PAS; Benítez et al. 2009, 2014) is poised to overcome the problems associated with broad and narrow band photometric surveys. J-PAS will be a very powerful tool in detecting galaxy clusters and providing new clues for the understanding of the role of dense environment in quenching star formation in galaxies. J-PAS is a photometric survey that will scan thousands of square degrees of the sky. With its 54 narrow-band filters ($FWHM \sim 145$ Å, with a difference of ~100 Å between

the central wavelength of each one), plus two medium and four broadband filters, it will provide data of a scope that is comparable to very-low-resolution spectroscopy ($R \sim 60$, $\Delta\lambda \sim 100\,\text{Å}$).

J-PAS is ideal for studies focused on the role of environment in galaxy evolution thanks to its capability to detect galaxy clusters and groups (see González Delgado et al. 2022). It will be able to provide robust cluster or group detection based on accurate photometric redshifts (Hernán-Caballero et al. 2021).The sensitivity of the survey allows us to easily observe the whole galaxy cluster memberships brighter than 22.5 in r band and to study the quenching as a function of cluster-centric radius. J-PAS is ideal for SED fitting and for identifying and characterise the blue and red galaxy populations (González Delgado et al. 2021). Given its spectral coverage and resolution, it is capable of identifying emission line objects and also measuring the lines Hα, [NII]$\lambda6584$, Hβ, and [OIII]$\lambda5007$ in clusters at $z < 0.35$ (Martínez-Solaeche et al. 2021, 2022). These lines are relevant to discriminate between the AGN and star-forming (SF) populations and to study their spatial distribution within the cluster.

At present, there is data available using the J-PAS photometric system: miniJPAS (Bonoli et al. 2021). In this paper, we identify the galaxy populations to study the variation of galaxy properties as a function of the cluster-centric radius in the largest cluster detected in miniJPAS, mJPC2470-1771. The ultimate goal is to demonstrate the capability and the power of J-PAS for investigating the characterisation of galaxy populations in galaxy clusters, as well as the role of environment in quenching the star formation. This will allow us to shed light on the processes responsible for transforming blue and star-forming galaxies into red galaxies in this dense environments.

This paper is structured as follows. In Sect. 2, we briefly summarise the miniJPAS observations and calibrations as well as the selection of the cluster members. In Sect. 3, we describe the methods used to identify and study the stellar population properties of the galaxies and we compare the results obtained with different photometries. In Sect. 4, we present the stellar population properties of these galaxy populations, we divide our ELG into star-forming (SF) galaxies and galaxies with an active galactic nuclei (AGN), and we study the SFR of the cluster galaxies. In Sect. 5, we discuss our results in terms of their spatial and radial distributions and in Sect. 6, we summarise our results and present our conclusions.

Throughout this paper, we assume a Lambda cold dark matter (ΛCDM) cosmology with $h = 0.674$, $\Omega_M = 0.315$, $\Omega_\Lambda = 0.685$, based on the latest results from Planck Collaboration VI (2020). This is the same cosmology used by Bonoli et al. (2021). We use the AB magnitude system Oke & Gunn (1983). We use the standard notation M_Δ for the mass enclosed within a sphere of radius R_Δ, within which the mean overdensity equals $\Delta \times \rho_c(z)$ at a particular redshift z; that is, $M_\Delta = (4\pi\Delta/3)\rho_c(z)R_\Delta^3$.

2. Data: miniJPAS

2.1. Observations and calibration

The miniJPAS survey (Bonoli et al. 2021) is a $1\,\text{deg}^2$ imaging survey performed at the Observatorio Astrofísico de Javalambre, (OAJ, Cenarro et al. 2014) using the 2.5m Javalambre Survey Telescope (JST/T250, Cenarro et al. 2018), which provides a good image quality along the optical spectral range (3300–$11\,000\,\text{Å}$). The instrument used for the data acquisition is the JPAS-Pathfinder camera. It has a single charge-coupled device (CCD) with $9.2\text{k} \times 9.2\text{k}$ pixel. The resulting field of view (FoV) is $0.27\,\text{deg}^2$ and the pixel scale is $0.23''\,\text{pixel}^{-1}$.

The survey consists of four pointings along the AEGIS stripe (Davis et al. 2007).

One of the greatest strengths of J-PAS resides in its photometric system. It consists of 54 narrow-band (NB) filters with a full width at half maximum (FWHM) of $145\,\text{Å}$ spaced by $100\,\text{Å}$, covering the spectral range from $3780\,\text{Å}$ to $9100\,\text{Å}$. There are two broader filters complementing these NB ones: u_{JAVA}, a medium band filter with FWHM of $495\,\text{Å}$ and centred at $3497\,\text{Å}$ and J1007, a high-pass filter centred at $9316\,\text{Å}$. This system provides low-resolution spectra ($R \sim 60$), referred to as J-spectra, and allows us to detect, identify, and characterise the stellar population properties of galaxies up to $z \sim 1$ (González Delgado et al. 2021). The filter system was originally optimised to accurately measure photometric redshifts (photo-z) for cosmological studies (Benítez et al. 2009, 2014; Bonoli et al. 2021). In addition, four SSDS-like broadband filters are included: u_{JPAS}, g_{SDSS}, r_{SDSS}, and i_{SDSS}. In particular, r_{SDSS} is used as the reference detection band for the miniJPAS 'dual-mode' catalogues. More information about the filter system can be found in Marín-Franch et al. (2012) and Bonoli et al. (2021).

The area observed in miniJPAS overlaps with the AEGIS field, which is located in the north galactic hemisphere with coordinates: $(\alpha, \delta) = (215.00°, +53.00°)$. It is composed of four pointings covering a total area of $1\,\text{deg}^2$. The depth is deeper than 22 mag for filters with $\lambda < 7500\,\text{Å}$ and is ~22 mag for longer wavelengths. The data was processed by the Data Processing and Archiving Unit (UPAD, Cristóbal-Hornillos et al. 2014) at Centro de Estudios de Física del Cosmos de Aragón (CEFCA). Further details on the different processes involved (the processing of single images, the final coadded images, the PSF treatment, the photometry and its calibration, and the masks) can be found in Bonoli et al. (2021). Nonetheless, the data used in this work was obtained with SExtractor dual-mode (Bertin & Arnouts 1996). The photometric calibration is an adaptation of the methodology presented in López-Sanjuan et al. (2019). All the images and catalogues are available through the CEFCA Web portal[1], which also offers advanced tools for data searches, visualisations, and data queries (see Civera & Hernández 2020, and a future paper is also forthcoming; Civera et al., in prep.).

2.2. Identification of galaxy members

The reference code for the detection of galaxy clusters in this work is Adaptive Matched Identifier of Clustered Objects (AMICO, Maturi et al. 2005; Bellagamba et al. 2018a), which is an algorithm based on the optimal filtering technique (see e.g., Postman et al. 1996; Bellagamba et al. 2011, 2018b). It uses a statistical description of the background noise and a template to characterise the signal of the clusters. The signal is defined as the product of the template and an amplitude, plus the noise component. It uses several inputs, mainly the galaxies' sky positions, their magnitudes, and their redshifts, to compute this amplitude and other parameters. Our parameter of interest is the association probability assigned to each galaxy, which represents the probability of the galaxy of being a member of the cluster. All the details and AMICO inputs used for making this catalogue of galaxy clusters in miniJPAS will be detailed in a forthcoming work (Maturi et al., in prep.).

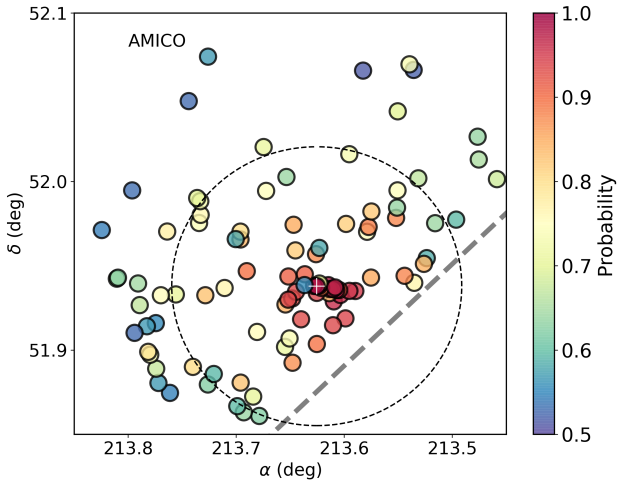For this work, we use the results from AMICO when using the PHOTOZ (the redshift corresponding to the maximum

---

[1] https://archive.cefca.es/catalogues

Fig. 1. Galaxy members of mJPC2470-1771 in the sky plane. The colour bar indicates the AMICO probability of being a member galaxy. The grey dashed line indicates the edge of the field of view of mini-JPAS. The black dashed circle indicates the value of R_{200}. The white cross represents the position of the BCG.

of the redshift probability density function, zPDF see Hernán-Caballero et al. 2021). The choice of the redshift affects the galaxy members identified for the cluster, but for our purpose (the identification and characterisation of the galaxy populations in mJPC2470-1771), there are no significant differences (see Appendix A). We used this catalogue since it is based on the same redshift as the one used for the SED-fitting analysis carried out by González Delgado et al. (2021) using BaySeAGal (see Sec. 3.1).

The cluster, mJPC2470–1771, was identified as the most massive in miniJPAS by Bonoli et al. (2021). The redshift of the cluster is $z = 0.29$. In total, there are 99 objects (see Fig. 1) with AMICO association probability higher than 0.5 and brighter than 22.5 in the r band. We identify the brightest cluster galaxy (BCG) as the galaxy with the highest luminosity in the r_{SDSS} and the highest stellar mass. Its ID in the miniJPAS catalogue is 2470-1771 and its coordinates are $(\alpha, \delta) = (213.6254°, +51.9379°)$.

The catalogue of this cluster has been tested with the follow-up on Gemini/GMOS observation of 38 galaxies with probabilistic association larger than 0.5 (Carrasco et al., in prep.). Two galaxies failed to be classified by AMICO as members of the cluster, which have probabilities 0.58 and 0.62 in the catalogue. Therefore, we estimated that AMICO classification only fails in 5% of cases.

Using GMOS spectroscopy, we estimated that R_{200}[2] is 1304 kpc, and the halo mass is $M_{200} = 3.3 \times 10^{14}\ M_\odot$. These estimates are based on the measurement of the velocity dispersion. The measurement took all the observed members and applied the Clean routine from Mamon et al. (2013) on it. This routine iteratively estimates the velocity dispersion and removes the outliers based on the caustic profile. Velocity dispersion is estimated using MAD (Beers et al. 1990). Using this value of R_{200}, we see that some members of the cluster may be outside of our observing FoV (see Fig. 1).

In fact, assuming that galaxies are symmetrically distributed up to R_{200}, we estimated that nine galaxies that are between $0.5R_{200}$ and R_{200} may not be included in our observing FoV.

---

[2] R_{200} is the radius where the mean mass overdensity is 200 times the critical density at the cluster's redshift.

These galaxies represent only 12% of the sample; thus, any conclusion within R_{200} is robust. Outside R_{200}, the incompleteness could be higher, but it is difficult to evaluate, and could be up to ~20–30% if the galaxy members show a circular symmetry. Thus, conclusions outside R_{200} must be taken with caution. In any case, extensive properties, such as the stellar mass surface density, are corrected for this incompleteness.

The cluster has also been detected with other IDs, such as MaxBCG J213.62543+51.93786 (Koester et al. 2007), who found a detected richness of 19 (scaled richness 17); WHL J141430.1+515616 (Wen et al. 2012), who found a R_{200} of 1.2 Mpc, 30 objects inside R_{200}, and a richness of 34, or RM J141430.1+515616.5 (Rozo et al. 2015a,b). None of these works are dedicated to a specific study of the properties of the galaxy members of this cluster; moreover, they are incomplete in their detection memberships. Thus, our work is the first and almost complete (~10% outside of the FOV) study inside R_{200} for cluster memberships brighter than 22.5 (AB) in the r-band.

2.3. Observational properties of galaxy members

We have two different available photometries, MAG_AUTO and MAG_PSFCOR. The first one is provided by SExtractor and estimates the total flux of the galaxy using an adaptive scaled aperture (see Bertin & Arnouts 1996, and SExtractor manual for further details.). Using the same approach as Molino et al. (2019), MAG_PSFCOR is aimed at correcting for the differences in PSF among different bands. It uses an aperture with the same shape as the Kron radius (smaller than the one used by MAG_AUTO) to provide robust colours determination (see Bonoli et al. 2021, for further details). Due to their different apertures and extraction procedures (Bonoli et al. 2021), results between both may vary from one galaxy to another. In particular, MAG_AUTO uses a larger aperture, so it may include outer regions of the galaxy in the integration process, which tend to contain younger, blue stars. In fact, González Delgado et al. (2021) compared the values of the stellar population properties obtained fitting the data from MAG_AUTO and MAG_PSFCOR, finding that the main difference is that, on average, masses are 0.2 dex larger in MAG_AUTO and rest frame colours are also bluer by −0.09 mag. Therefore, for our analysis, we used MAG_PSFCOR, given its better signal-to-noise ratio (S/N). Its smaller aperture also allows for an improved detection of the emission lines in the centre of the galaxies.

We first looked at the observational properties of the galaxies (see Fig. 2). The median measured redshift of the cluster's galaxies is $z = 0.29$, with a standard deviation of $\sigma = 0.02$. There are four galaxies with redshift greater than 0.35. We looked at the zPDF of the galaxies in the galaxies in the cluster. These four galaxies are the only ones that show a multimodal distribution with peaks of similar amplitude (more than ~50% of the amplitude of the maximum peak). Due to their zPDF and their PHOTOZ, we decided to remove these four galaxies from our analysis.

The distribution of r_{SDSS} peaks at around ~21 mag and most galaxies are brighter than 22.5 mag. The number of galaxies in each bin steeply decreases with increasing median S/N, but the peak of the distribution is close to 10. We see that brighter galaxies have a better S/N. Although there are galaxies with different probability and brightness, most of the galaxies with probability higher than ~0.8 have a magnitude brighter than 20 and a S/N higher than ~11. On the other hand, galaxies with probability lower than ~0.6 have a S/N higher than ~10.
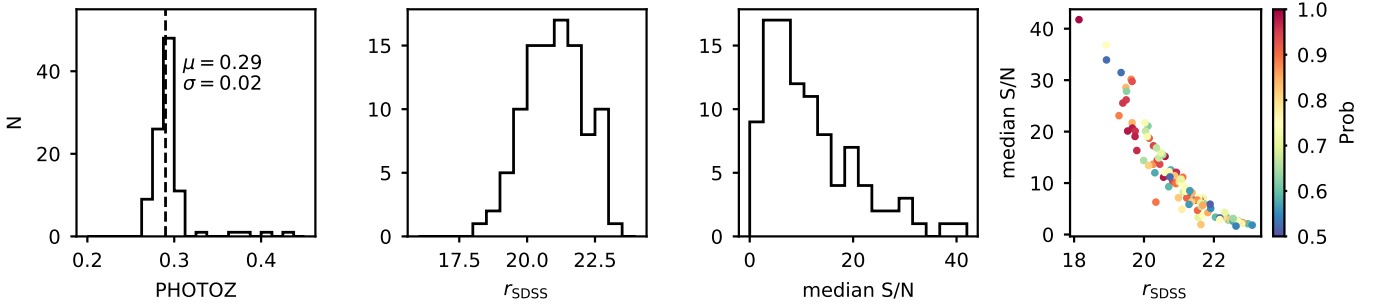
Fig. 2. Observational properties of the galaxies in the cluster. *First panel*: redshift (PHOTOZ) distribution. The median (μ) and standard deviation (σ) of PHOTOZ are written in the figure. The black dashed line represents the median of PHOTOZ. *Second and third panels*: distributions of the r_{SDSS} magnitude, and median S/N of the narrow-band filters. *Fourth panel*: median MAG_PSFCOR S/N in the narrow-band filters as a function of r_{SDSS} magnitude. Colour coding indicates the probabilistic association given by AMICO.

3. Identification of the galaxy populations

The purpose of this section is to identify the red (RG), blue (BG), and emission line (ELG) galaxies in the cluster. First, we explain the method for retrieving the stellar population properties of the galaxies based on the J-spectra fits. Then we describe the methods to identify ELGs.

3.1. J-spectra fits

We used BaySeAGal (de Amorim et al., in prep.), a parametric SED fitting code, to obtain the stellar population properties from J-spectra. BaySeAGal is an adaptation of the method developed by López Fernández et al. (2018) in order to use J-PAS magnitudes as input. The code generates synthetic J-spectra from parametric SFH models. For a given observed J-spectra we performed a Markov Chain Monte Carlo (MCMC) exploration of the parameter space, thus obtaining a sample of parameters that approximates the probability density function (PDF) of the model. In this work we assumed a delayed-τ model given by:

$$\psi(t) = \frac{M_{ini}}{\tau^2 \left[1 - e^{-\frac{t_0}{\tau}} \left(\frac{t_0}{\tau} + 1\right)\right]} (t_0 - t) e^{-\frac{t_0 - t}{\tau}}, \tag{1}$$

where t is the look-back time, t_0 is the (look-back) time when the star formation began, τ is a measurement of how extended in time the star formation was, and M_{ini} is the total mass of formed stars. This model also includes stellar metallicity (Z) and dust attenuation (A_V) which, combined with stellar population model spectra and a foreground dust screen extinction curve, results in a set of model J-spectra[3]. The complete set of parameters is (t_0, τ, A_V, Z). We also obtained the stellar mass ($M_\star$) from the scaling factor of the model with relation to the observed J-spectra. From these parameters, we can calculate the mass-weighted and light-weighted ages and rest-frame colours.

We let 100 chains walk the parameter space for 2200 steps. The autocorrelation time[4] of the chains for this model is around 120 steps, we discarded the first 1200 steps as a burn-in phase. In the end, we got a total of 100 000 samples of the parameter

space. For each galaxy, we took the mean and standard deviation of the parameters and properties of the samples as an estimate of their expected value and uncertainties.

Emission lines are not included in the models. Because some of the NBs can be affected by strong contributions from the Balmer (Hα, Hβ) and optical collisionally-excited ([OIII]λ5007, 4959, [OII]λ3727, [NII]λ6589, 6548) emission lines, we removed those bands where these lines could be at the redshift of each galaxy from the fits. In this way, we ensure that the fit is done only over the stellar continuum since the nebular continuum is negligible in most of the SF galaxies. Only objects with HII regions with very extreme emission lines (e.g., EW(Hα) > 1000 Å Gonzalez Delgado et al. 1994) would be affected by this assumption. These galaxies are not present in this sample.

A more detailed explanation of the method with a global study of the galaxies in the AEGIS field can be found in González Delgado et al. (2021). Since the data used in this paper are a subsample from González Delgado et al. (2021), the models are computed using the initial mass function (IMF) by Chabrier (2003) and the latest versions of the Bruzual & Charlot (2003) stellar population synthesis models (Plat et al. 2019). We chose the attenuation law by Calzetti et al. (2000) which we added as a foreground screen. We also note that, unless stated otherwise, the term 'mass' refers to the stellar mass ($M_\star$) derived by BaySeAGal.

In Fig. 3, we show the J-spectra of six galaxies (three red and three blue) along with the fits obtained with BaySeAGal. These galaxies are identified with red and blue circles in the top panel. This serves as an example of the aspect of J-PAS data, the effectiveness of BaySeAGal and it also manifests the capability of J-PAS to detect line emission (which will be exploited in Sect. 3.3).

3.2. Identification of red and blue galaxies in the cluster

Throughout this paper, we use two different colours: $(u - r)_{res}$ and $(u - r)_{int}$. Both of them are rest-frame colours derived from the star formation history obtained from the SED fitting (see Sect. 3.1), but the first one is not corrected from extinction while the second one is calculated including the reddening correction in the synthetic SED.

The bimodal distribution of the AEGIS galaxy population is shown in the galaxy stellar mass-colour diagram (González Delgado et al. 2021). In this work, we show that $(u - r)_{int}$ is more useful than $(u - r)$ to discriminate between the red star-forming and quiescent galaxies because it accounts for

---

[3] The stellar population spectra are preprocessed and converted to observed-frame magnitudes for a grid of redshifts, using J-PAS filter curves.

[4] The assessment of autocorrelation time and convergence of the chains was performed in a small sample of J-spectra. This is a fairly manual process, as with any MCMC convergence study. We consider the burn-in phase to be over at around 5× the autocorrelation time, which we assume is conservative enough.
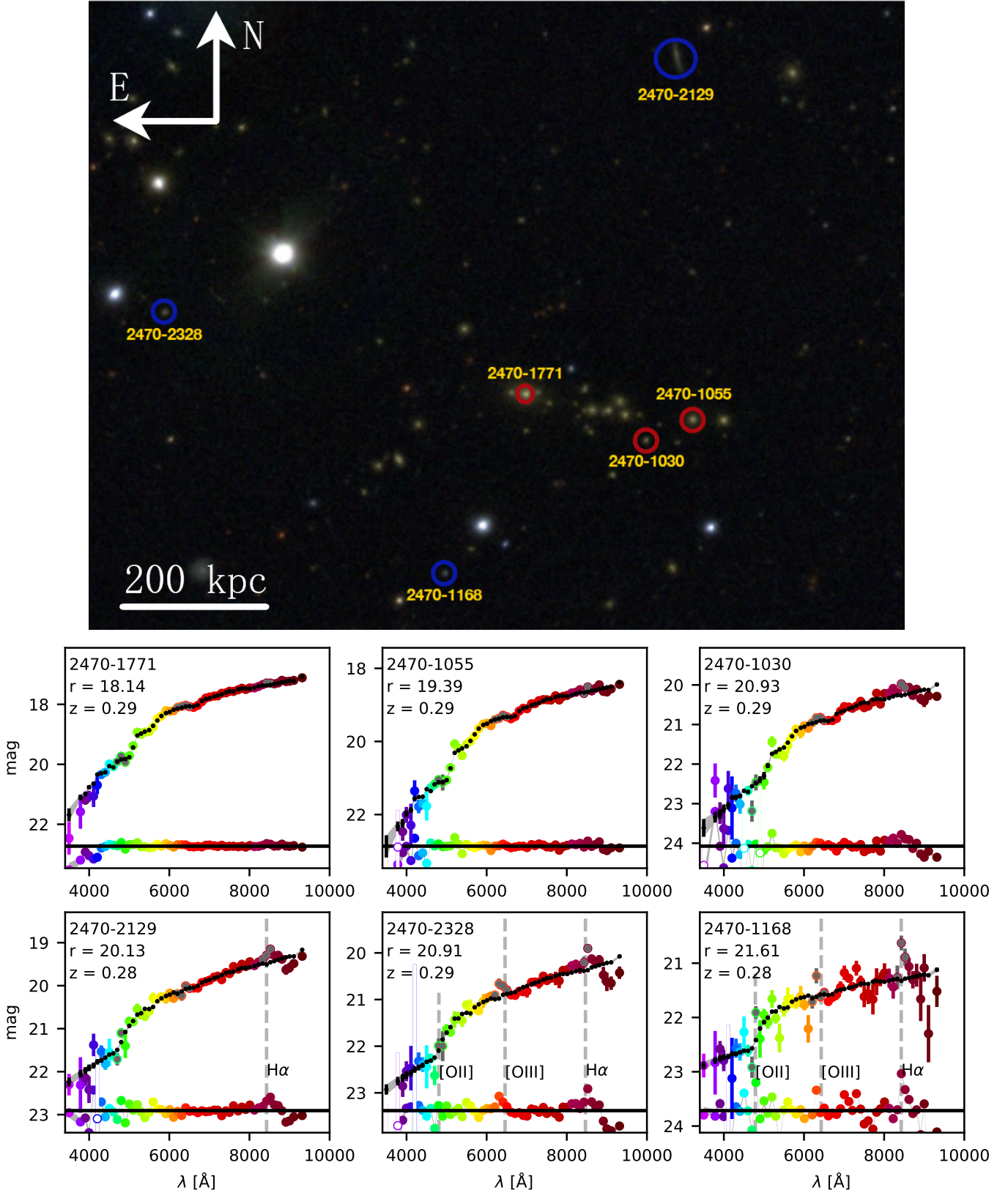
Fig. 3. mJPC2470-1771 and J-spectra examples. *Top panel*: miniJPAS view of mJPC2470-1771. Prominent red and blue galaxies in the cluster are marked with red and blue circles, respectively. The BCG corresponds to 2470-1771, with an spectroscopic redshift of $z = 0.289$. *Bottom panel*: `MAG_PSFCOR` J-spectra of three red galaxies (top row) and three blue galaxies (bottom row) that are marked with circles in the top panel. The mean model fitted by `BaySeAGal` is plotted as black points, and the grey band shows the magnitudes of the mean model $\pm$ one σ uncertainty level. The difference between the model and the best model fitted magnitudes are plotted as a small coloured points around the black bottom line. Masked filter (white coloured circles) and filters overlapping with the emission lines Hα, [NII], [OIII], Hβ, and [OII] (darker grey coloured circles) are not used in the fit. Grey vertical dashed lines show the wavelengths corresponding to detectable emission lines.

the fraction of red star-forming galaxy population of the sample. We use an adaptation of the criterion given by Díaz-García et al. (2019), previously been used by González Delgado et al. (2021) to segregate the whole galaxy populations in miniJPAS in red and blue galaxies. We consider galaxies to be red if:

$$(u - r)_{\text{int}} > 0.16(\log(M_\star) - 10) - 0.254(z - 0.1) + 1.792, \quad (2)$$

and blue otherwise.

3.3. ELG identification

As seen in Fig. 3, the J-spectra are capable of showing the line emission as excess flux in a given filter. In this section, we describe two methods for classifying the galaxies as emitters or non-emitters, with respect solely to the Hα emission. We applied the methods to the cluster catalogue to characterise the emission line galaxy populations.

3.3.1. Median error method

This method is based on our miniJPAS data but also uses a prior based on the result from our SED fitting code, since we distinguish between red and blue galaxies. The base idea is that when looking at the filter that is sensible to the observed line wavelength, a galaxy that presents Hα (or Hα +[NII], as in this method we cannot separate the emission of both lines) emission will show a lower magnitude value in the observed J-spectra (m_{obs}) than in the stellar continuum fit (m_{fit}). However, it is not enough to simply consider that $m_{\text{fit}} - m_{\text{obs}} > 0$. We must establish a threshold value. A first consideration to make is that the difference must be greater than the observed error. In order to estimate the observed error of the fitted stellar continuum, we consider the median error in the five filters closer to the band where Hα is, symmetrically distributed. If we only choose three filters, our estimation could be contaminated with other lines close to Hα, such as [SII]. Choosing seven filters only changes the final set in one galaxy. Choosing more filters would mean estimating the continuum too far from Hα, given the width of J-PAS filters. Besides, the blue galaxies in our sample are noisier than red galaxies. The median S/N in the five closest filters to Hα at the cluster redshift is almost three times better for red galaxies than for blue galaxies. We find that the larger magnitude difference of the blue galaxies is not enough to compensate their worse S/N. This implies that if the same threshold (three sigma) is applied, there will be a bias towards the detection of less blue emission line galaxies. Lastly, we must take into account that due to the uncertainties in the PHOTOZ determination, the filter with the closest central wavelength to the calculated line wavelength might not be the one showing the line emission. This is a consequence of our method being fine tuned to fit a set of galaxies observed with spectroscopy in the cluster area (see Appendix B). Therefore, our method proceeds as follows. First, we find the closest filter to the observed line wavelength. Then, we calculate the median error of that filter and the four adjacent ones (symmetrically distributed) $\eta(\epsilon_{m_{\text{obs}}})$. Finally, we look at the closest filter, the previous and the next one, and we classify the galaxy as an emission line galaxy if one of those filters satisfies the following condition:

$$m_{\text{fit}} - m_{\text{obs}} > \theta \cdot \eta(\epsilon_{m_{\text{obs}}}), \quad (3)$$

where $\theta = 1$ for blue galaxies and $\theta = 3$ for red galaxies in order to account for their better S/N in the filters closer to the Hα wavelength at the cluster redshift. These values of θ were chosen in

order to account for this differences in the S/N. They have been tested with the data from GMOS spectroscopic observations of 13 galaxies with clear Hα emission in the spectra.

This method allows us to identify emission line galaxies in the cluster, but we do not use it to estimate the fluxes of the lines; in this respect, the ANN method is more useful.

3.3.2. ANN

This method uses the equivalent width of Hα, EW(Hα) predictions made by Martínez-Solaeche et al. (2021) ANN. In that work, two different ANNs are trained using synthetic photometry (in the sense that real spectra are processed to obtain J-PAS magnitudes) obtained from the Calar Alto Legacy Integral Field Area survey (CALIFA, Sánchez et al. 2012) and the Mapping nearby Galaxies at Apache Point Observatory survey (MANGA, Bundy et al. 2015). One of the ANN is trained to calculate the EW of Hα, Hβ, [OIII], and [NII]. The other ANN is trained in order to classify the galaxies into ELG and quiescent galaxies. The CALIFA and MANGA galaxies contain millions of spaxels with different astrophysical conditions, which include regions with high and low star-formation activity as well as variations in the gas-phase metallicity or the dust distribution. Furthermore, CALIFA and MANGA survey contain galaxies in different environments (clusters, groups and field) since they were selected to avoid environmental bias (Walcher et al. 2014; Wake et al. 2017). Therefore, we do not expect our prediction to be unlikely in the cluster under study. Nevertheless, by construction, our training set includes, on average, a smaller amount of spaxels ionized by the presence of AGN or shocks waves. In Martínez-Solaeche et al. (2021) we showed that we do not miss a fraction of AGN larger than 3% over the whole sample of galaxies used from SDSS. This confirms that the transfer from the training sample to our current data is trustworthy.

As explained in Martínez-Solaeche et al. (2021), there is a minimum measurable EW for a photometric filter. Therefore, the criteria we use is simply to consider the galaxy as an emission line galaxy if the EW given by the ANN is greater than the minimum measurable EW, taking the error bars into account. This is:

$$\frac{\Delta'}{S/N - 1} < \text{EW}_{\text{H}\alpha_{\text{ANN}}} + \epsilon\text{EW}_{\text{H}\alpha_{\text{ANN}}} \; ; \; \text{EW}_{\text{H}\alpha_{\text{ANN}}} > \epsilon\text{EW}_{\text{H}\alpha_{\text{ANN}}},$$

where Δ' is the equivalent width of the filter and can be calculated as:

$$\Delta' = \frac{\int \lambda T(\lambda) \mathrm{d}\lambda}{\lambda_z T(\lambda_z)}, \quad (4)$$

where T is the normalised transmittance of the filter and λ_z is the observed emission line wavelength. To compute the minimum measurable EW, we find the J-PAS filter with a central wavelength closest to the observed Hα wavelength given the galaxy's redshift. Since the minimum EW is associated with a certain filter, the Δ' and S/N parameters must be considered in the same filter and it does not make any sense to consider a median value for any of them. Also, since we are using the ANN predictions, here we can separate the Hα emission fom the [NII] emission.

This method is very useful not only for identifying emission line galaxies, but also to predict the EW of Hα, Hβ, [NII], and [OIII] lines, along with their respective ratios ([NII]/Hα, [OIII]/Hβ). We are able to reach a precision in the log([NII]/Hα) of 0.09 dex for SF galaxies and average $S/N \sim 10$ in the J-spectra. This is independent of the redshift of the galaxies as we prove in (Martínez-Solaeche et al. 2021), where we tested

our results with a sample of SDSS galaxies within the redhisft range of $0 < z < 0.35$.

3.3.3. ELG final set

We then applied both methods to all the galaxies in the cluster. The median error method selects 57 galaxies as galaxies with emission lines, while the ANN method selects 50 galaxies in total. We decided to be more conservative and consider as ELG population the intersection of both groups, since this defines a more robust subset. A total of 49 galaxies remains. A comparison of the three sets with the whole cluster colour distribution can be seen in Fig. 4. The $(u - r)_{int}$ distribution is very similar in both methods, peaking around $(u - r)_{int} \approx 1$ and with a lower peak at $(u - r)_{int} \approx 2.2$. This peak is easily understood when looking at the general distribution, since there is also a peak at this value, even greater than the bluer one. When defining the median error method and establishing the values of the multipliers, there is a risk of generating a greater bias towards blue galaxies greater than desired in order to account for the larger errors. Comparing its histogram with the ANN, we can see that the proportion of blue and red galaxies remains very similar, so we can trust this method. As a final comment, these results are coherent with what we would expect, since most of the ELG are blue.

4. Characterisation of the galaxy populations

In this section, we analyse the stellar population properties of the galaxies belonging to the cluster. First, the sample is divided in red and blue galaxies. Then, ELG are characterised by their stellar populations by dividing also the galaxies in star-forming (SF) and galaxies with an active galactic nucleae (AGN). The average and dispersion values of the stellar population properties are summarised in Table 1.

4.1. The red and blue galaxy populations

The bimodal distribution of the red and blue galaxies in the cluster can be seen in the colour-mass diagram (see Fig. 5) The comparison between the $(u - r)_{res}$ and the $(u - r)_{int}$ shows how the extinction correction moves a significant number of galaxies from the redder (upper) regions of the diagram to the bluer regions (below the black dashed line). The colour code also shows how, on average, redder galaxies are older and more metal-rich. Galaxies with larger extinctions are located in the middle region of the diagram, which could be considered as an equivalent of the green valley. The comparison with González Delgado et al. (2021) results for the whole AEGIS catalogue shows that the distribution of these properties in the colour-mass diagrams remains the same. This would indicate that, for fixed values of the colour and mass, the effect of the environment on these properties is negligible. We find that, on average, red galaxies are more massive than blue galaxies by ∼0.8 dex. Blue galaxies also show a larger variance in mass. The extinction A_V is significantly larger on average (∼0.5 mag) for blue galaxies. This is expected because most of the blue galaxies are star-forming, and the extinction that young stars experience is almost double than that for the old stellar population (Charlot & Fall 2000). In contrast, blue galaxies are less metal rich than red galaxies by ∼0.1 dex. On average, red galaxies are older by 0.4 dex. The value of τ/t_0 is nine times larger for blue galaxies than for red galaxies; thus, the star formation lasts longer in the blue galaxy population.
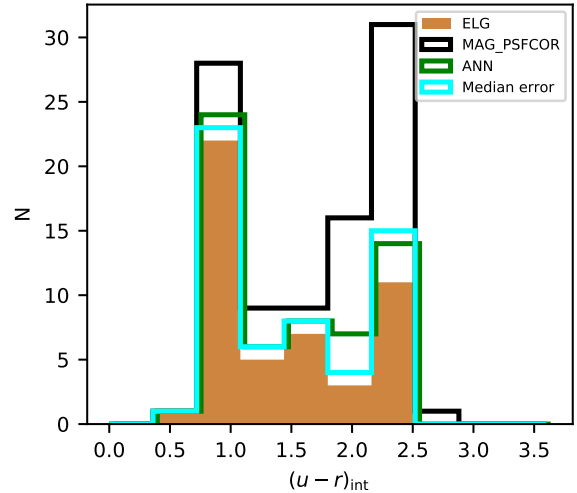

Fig. 4. $(u - r)_{int}$ histogram comparing the emission line galaxies selection criteria. The black line shows the distribution of all the galaxies in the AMICO catalogue. Cyan histogram shows the distribution for the median error. Same for green but with the ANN method. Orange solid histogram shows the distribution for the common galaxies for both methods. The different distributions have been shifted a little bit in the plot to show more clearly the similarities and differences between them.

The total fraction of red galaxies is 0.52 (0.48 for blue galaxies). The fraction of red galaxies in the whole catalogue of miniJPAS at the cluster's redshift, obtained by González Delgado et al. (2021), using BaySeAGal, is around 0.2 or even lower. This is supported by works in the literature such as Balogh et al. (2004). If we assume a symmetric distribution within R_{200}, and if all the missing galaxies were blue (worst case scenario), the fraction of red galaxies inside R_{200} would be 0.55 (compared to the current observed fraction of 0.62 inside R_{200}), which is still higher than the fraction of red galaxies in the field. Instead, if we assumed a symmetrical distribution keeping the same amount of blue and red galaxies in the missing area, we would find the fraction of red galaxies to be even larger (0.64).

4.2. ELG population

In Fig. 6 we compare the distribution of the stellar properties of the ELG with the whole sample and we summarise them in Table 1. We find that their values span the same ranges than the properties of the whole catalogue. However, the distribution themselves are different. The stellar mass still peaks at $\log M_\star \approx 10.5 \, [M_\odot]$, but the contribution of galaxies with $\log M_\star < 10 \, [M_\odot]$ becomes more significant. In fact, most of the galaxies in such range are classified as ELG. On average, ELGs are less massive than the whole sample by 0.1 dex. The distribution of A_V shows that most of the galaxies that are not selected as ELG exhibit values lower than 0.5, but the distribution remains similar (the average only becomes 0.06 mag lower). A similar behaviour is found for the metallicity, where most of the galaxies with $\log Z_\star \lesssim -0.5$ are ELG, but the peak of the distribution is still the same as the whole set. The average only becomes lower by 0.04 dex. Nonetheless, the distribution of $(u - r)_{res}$ changes significantly. The peak of the distribution is still found at $(u - r)_{res} \approx 2.5$ mag, but most of the galaxies with $(u - r)_{res} < 2$ are ELG, and only a few galaxies with $(u - r)_{res} > 2$ are ELG. Moreover, the peak of the stellar ages is now found at $\langle \log age \rangle_M \approx 9.25$, with most of the young galaxies being ELG

Table 1. Mean and standard deviation values of the stellar population properties of the galaxies in the cluster.

Property	Galaxies	RG	BG	ELG	ELG-R	ELG-B	SF	AGN
$\log M_\star$	10.0 ± 0.65	10.4 ± 0.32	9.63 ± 0.64	9.89 ± 0.71	10.5 ± 0.36	9.62 ± 0.65	9.56 ± 0.60	10.5 ± 0.42
A_V	0.57 ± 0.43	0.32 ± 0.19	0.84 ± 0.44	0.63 ± 0.42	0.32 ± 0.25	0.76 ± 0.40	0.65 ± 0.41	0.49 ± 0.35
$\log Z_\star >$	0.09 ± 0.45	0.29 ± 0.20	-0.1 ± 0.53	0.05 ± 0.50	0.35 ± 0.19	-0.0 ± 0.54	-0.0 ± 0.53	0.35 ± 0.25
$(u-r)_{\rm res}$	2.04 ± 0.51	2.42 ± 0.10	1.64 ± 0.48	1.85 ± 0.55	2.43 ± 0.08	1.59 ± 0.47	1.60 ± 0.50	2.31 ± 0.28
$(u-r)_{\rm int}$	1.67 ± 0.60	2.21 ± 0.16	1.10 ± 0.30	1.44 ± 0.58	2.22 ± 0.16	1.09 ± 0.30	1.18 ± 0.46	1.98 ± 0.43
$\langle \log age \rangle_{\rm M}$	9.44 ± 0.24	9.61 ± 0.13	9.26 ± 0.21	9.34 ± 0.23	9.53 ± 0.17	9.26 ± 0.21	9.27 ± 0.23	9.47 ± 0.22
τ/t_0	0.52 ± 0.60	0.12 ± 0.02	0.94 ± 0.63	0.71 ± 0.66	0.11 ± 0.02	0.97 ± 0.64	0.95 ± 0.68	0.23 ± 0.27

Notes. The properties are for red and blue galaxies (RG, BG), emission lines galaxies (ELG), ELG with red (ELG-R) or blue (ELG-B) colours, star-forming galaxies (SF), and galaxies with an AGN.

and only a few of the old galaxies showing emission lines (ELG are younger by 0.1 dex on average). Furthermore, most of the galaxies with $\tau/t_0 \lesssim 0.8$ are not ELG, and almost all the galaxies $\tau/t_0 \gtrsim 0.8$ are ELG, and the average value of ELGs is almost 50% larger than the average of the whole sample.

These results show that ELGs have properties similar to the BG population. However, they display differences that suggest that ELG is a mix of red and blue populations, where RG are significantly less abundant than the BG population. To further investigate this point, we explore the colour-mass diagram and the distribution of the inferred EW(Hα), dividing the ELG into red (ELG-R) and blue (ELG-B) galaxies (Fig. 7). We see that galaxies with the lowest predicted EW (<10 Å approximately) are all red galaxies, while galaxies above this value are all blue – except for three of them. Two of them are particularly notable, having a predicted EW above 50 Å. However, when looking at the spectra, we find that the inferred emission may be a result from incomplete background subtraction due to fringing effect that suffer some of the red filters, which is translated into a variation of the measured magnitude that could be interpreted as an emission line by the ANN, due to the magnitude difference among one filter and its adjacent ones. With that exception, we can conclude that ELG-R are characterised by low estimated values of EW(Hα), while ELG-B have EW(Hα) > 10 Å. Taking into account that our ELG-R are more massive than our ELG-B, we find that our results are coherent with the EW(Hα)-mass relation found in the literature (see e.g., Fumagalli et al. 2012; Sobral et al. 2014; Khostovan et al. 2021).

4.3. Star-forming galaxies and AGN populations

The ELG population can be a mix of star-forming galaxies (SF) and AGN galaxies. To find the abundance of these two classes, we use two different diagrams: the WHAN diagram, introduced by Cid Fernandes et al. (2010, hereafter CF10), and the BPT diagram (Baldwin et al. 1981). There are a number of works that present their own criteria to separate the SF, Seyferts and LINERs in the BPT diagram, but here we use the results from three in particular: Kauffmann et al. (2003a, hereafter K03) and Kewley et al. (2001, hereafter K01) to distinct SF galaxies from galaxies with a potential AGN, and we use the transposition to this diagram made by Cid Fernandes et al. (2010) of the separation criteria between Seyferts and LINERs found by Kewley et al. (2006, hereafter K06). In the case of the WHAN diagram, we use the criteria from CF10 and Cid Fernandes et al. (2011, hereafter CF11). In this work, several criteria are presented, but for consistency we choose the transpositions made in these works (CF10 and CF11) of the same criteria used in the

BPT (K03 and K01) in addition to the criteria of studies where galaxies with EW(Hα) < 3 Å are considered to be retired galaxies[5]. An example of each type of galaxy, with its J-spectra and its position in the WHAN and BPT diagrams, respectively, can be seen in Fig. C.1. This figure is useful to explain more clearly how we interpret the position of galaxies in these diagrams.

Figure 8 shows the WHAN and BPT diagrams with all the ELG population. Table C.1 shows the classification for each of these galaxies in both diagrams. Since a different classification can be derived from each diagram and due to the error bars obtained for many galaxies, it is not trivial to assign a label to each ELG. Therefore, we use a probabilistic approach in the following way: we calculate the area of the error box in the WHAN diagram and we calculate the fraction of this area that falls in each of the diagram regions. We define this fraction as the probability representing how likely it is for that galaxy to be a SF, Seyfert, LINER, retired, or composite (SF-Seyfert or SF-LINER) galaxy. The error bars plotted in this figure take into account the correlation among the emission lines through the calculation of the Pearson coefficient and its inclusion in the error budget.

We find that 32 galaxies (65.3% of the ELG) have a probability greater than 0.7 of being associated with the SF region (33 above 0.5, representing 67.3%). We selected these galaxies as the SF population. Only one galaxy (which represents 2% of the ELG) has a combined probability in the Seyfert and LINER region greater than 0.5 in the WHAN diagram. The rest of the galaxies are difficult to uniquely identify as AGN using only the WHAN diagram. Due to this restriction, we selected as AGNs those galaxies that are above the K01 curve in the BPT diagram if the probability of being SF in the WHAN diagram is less than 0.5. With these criteria, only 2470–3670 need to be excluded from the AGN sample (see Appendix C and Fig. C.1). Galaxies between the K01 and K03 lines likely have contributions from AGN, but we cannot resolve whether they are Syferts, LINERs, or composite galaxies. Thus, we do not include them as part of the AGN sample, nor as SF if they are not classified as SF in the WHAN diagram.

In Table 1, we summarise the stellar population properties of these galaxies. If we compare the SF galaxies with the blue ELG, we find that the differences in the average and standard deviation values are negligible except for the extinction A_V, which are lower for SF galaxies, and $(u-r)_{\rm int}$ colours, which are slightly redder (but with a greater standard deviation) for SF galaxies. This indicates that most of the blue ELG are SF galaxies.

---

[5] This is the name given by CF10 to red-quiescent galaxies with weak Hα emission, that is probably produced by post-AGB stars.
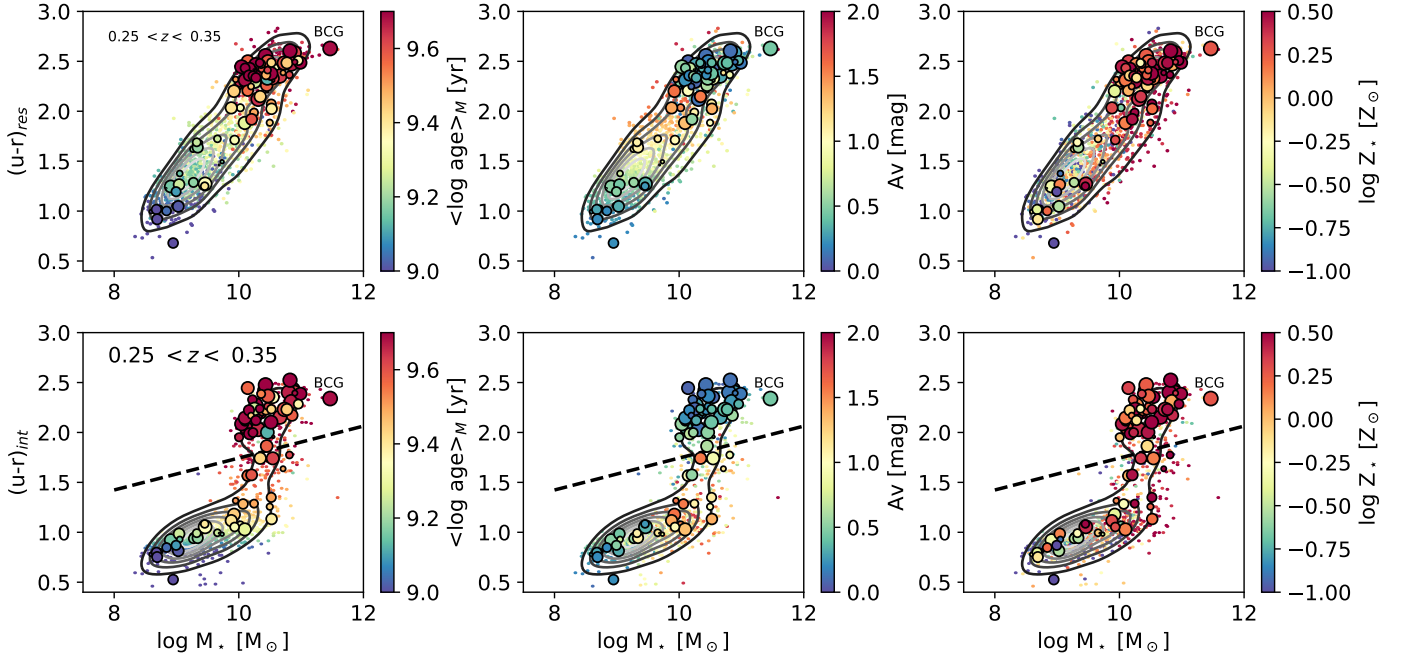
Fig. 5. $(u − r)_{\rm res}$ (*top panels*) and $(u − r)_{\rm int}$ (*bottom panels*) colour vs. stellar mass for the redshift bin $0.25 < z < 0.35$ derived by `BaySeAGal` from the AEGIS galaxy populations (contour) and galaxy cluster members (circles). The coloured bar shows the distribution of the stellar population properties age, extinction, and metallicity (*from left to right*). The size of the circles indicates the probability of the galaxy to be member of the cluster. The position of the brightest galaxy in the cluster (BCG) in each panel is marked. The dashed line in the $(u − r)_{\rm int}$ divides blue galaxies (below the line) and red galaxies (above the line).
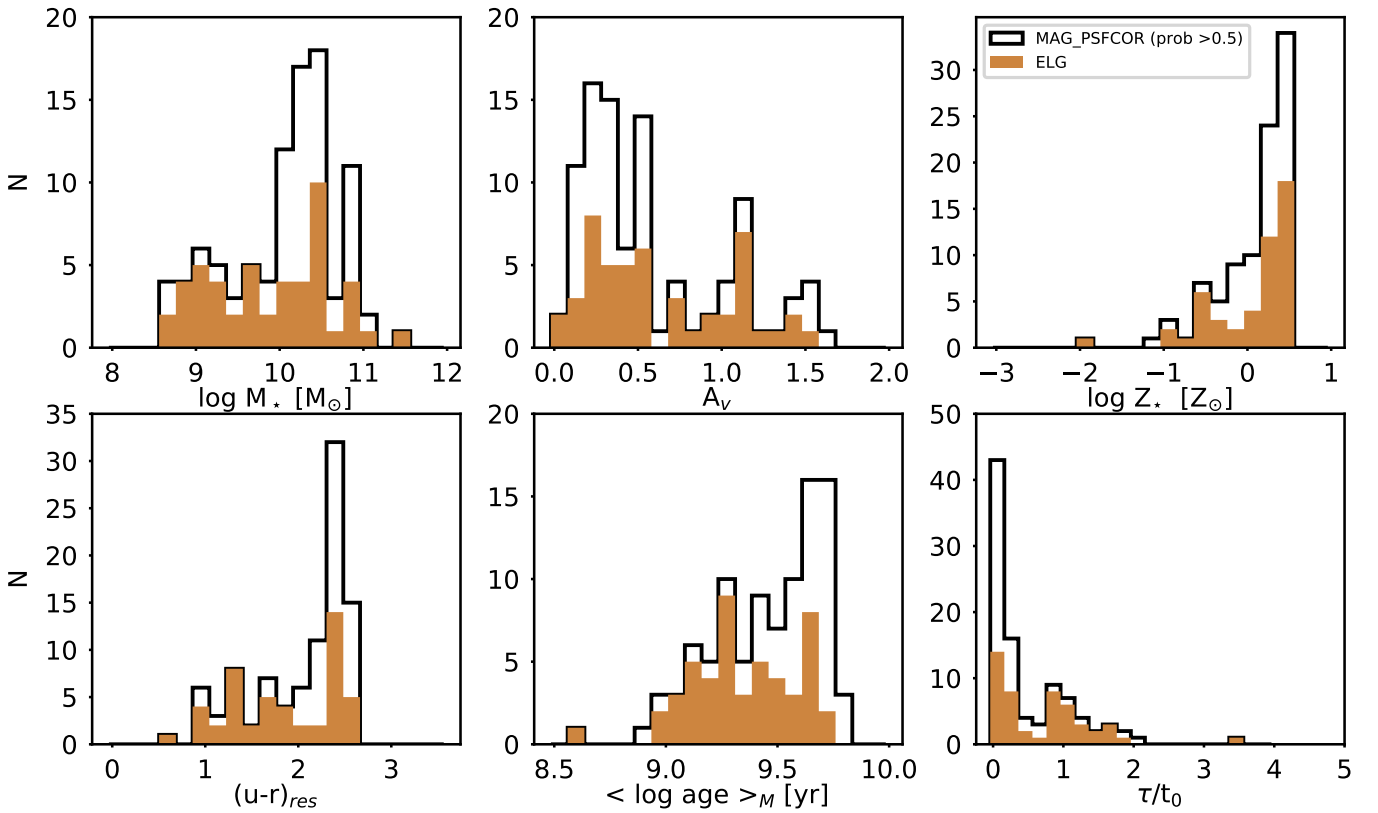
Fig. 6. Stellar population properties distribution for the emission line galaxy population. Black histogram shows the distribution for all the galaxy members in the `MAG_PSFCOR` photometry. Brown solid histogram shows the distribution for the objects selected as emission line galaxies. *From left to right and from upper to bottom*: stellar mass, extinction, stellar metallicity, $(u − r)_{\rm res}$ colour, mean mass-weighted age, and ratio between the SFR parameters τ and t0.
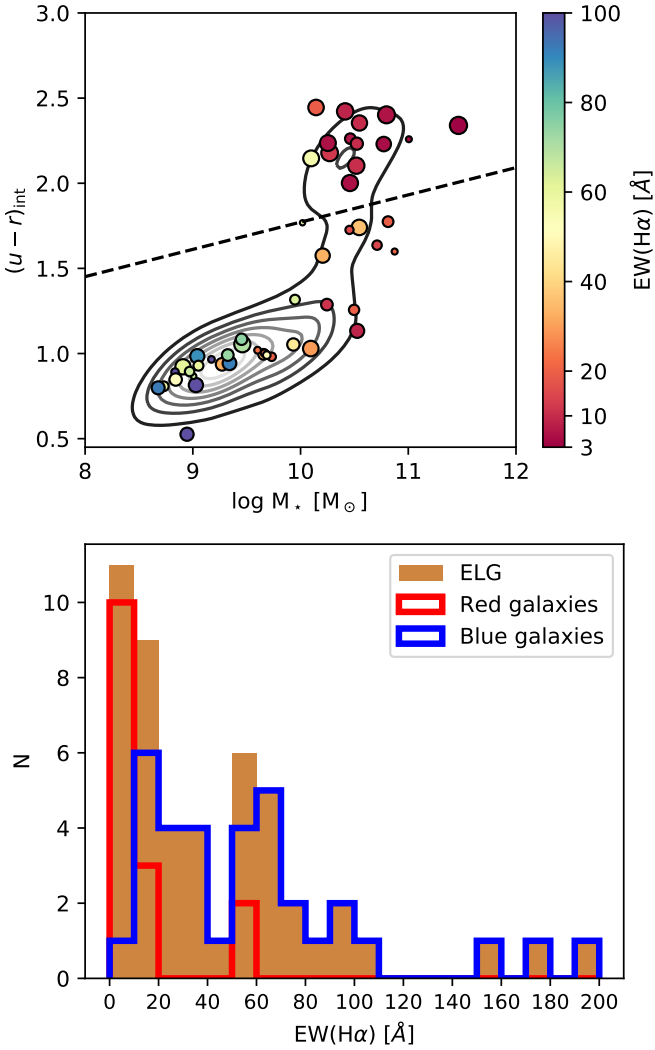
Fig. 7. EW(Hα) of the ELG population. *Top panel*: colour-mass diagram for the ELG galaxy population. The colour bar shows the Hα equivalent width. Galaxies above the black dashed line are considered to be red. Galaxies below are considered to be blue. *Bottom panel*: Hα equivalent width distribution histogram. Green histogram shows the distribution of the galaxies selected with the ANN method. Orange solid histogram shows the distribution for the selected galaxies. Red histogram shows the distribution of the selected red galaxies. The same holds true for blue histogram and blue galaxies.

The comparison between the values of the red ELG and AGN populations shows that the main difference between them resides in a larger extinction on average for the AGNs, slightly bluer $(u-r)_{res}$ and $(u-r)_{int}$ colours, younger ages and higher values of τ/t_0. This indicates that the sample selected as AGN is a mixture of blue and red ELGs and that we are not able to fully separate the contributions of pure AGNs from star formation in galaxies, or that most of these galaxies are actually composite.

We focus here on the Hα emission in order to select our ELG sample. This line can be used as a tracer of the star formation (see e.g., Kennicutt 1998; Kennicutt & Evans 2012; Kewley et al. 2002; Garn et al. 2010; Oteo et al. 2015; Catalán-Torrecilla et al. 2015) or the presence of AGNs (see e.g., Osterbrock & De Robertis 1985; Veilleux & Osterbrock 1987; Osterbrock 1989; Kewley et al. 2001; Cid Fernandes et al. 2011). Therefore, taking into account the relation between galaxies in the blue cloud and a higher star formation than galaxies in the red sequence, (see e.g., Kauffmann et al. 2003a,b; Baldry et al. 2004; Brinchmann et al. 2004; Gallazzi et al. 2005; Mateus et al. 2006, 2007), it is reasonable to assume that an important fraction of our selected ELG are blue galaxies, which are generally classified as star-forming galaxies according to the WHAN and BPT diagrams, and that red galaxies are generally classified as LINERS or retired galaxies. A similar discussion with compatible results can be found in the works of Chies-Santos et al. (2015), Rodríguez del Pino et al. (2017).

4.4. The star formation rate

In order to calculate the star formation rate (SFR) and the specific SFR (sSFR = SFR/$M_\star$), we use the star formation history (SFH), derived from the SED-fits to add up the stellar mass formed in the last 20 Myr and divide it by 20 Myr[6]. The mean and standard deviation values we obtain for the sSFR for each set of galaxies are $0.25 \pm 0.32\,\mathrm{Gyr}^{-1}$ for the whole sample, then $0.020 \pm 0.016\,\mathrm{Gyr}^{-1}$ for red galaxies, $0.49 \pm 0.32\,\mathrm{Gyr}^{-1}$ for blue galaxies, $0.35 \pm 0.35\,\mathrm{Gyr}^{-1}$ for the ELGs, $0.016 \pm 0.015\,\mathrm{Gyr}^{-1}$ for the red ELGs, $0.50 \pm 0.32\,\mathrm{Gyr}^{-1}$r for the blue ELGs, and $0.48 \pm 0.34\,\mathrm{Gyr}^{-1}$ for SF galaxies.

We find that the mean value of the sSFR of the blue galaxies is ~25 times larger than the mean value of the red galaxies. This is accordance with the literature (see e.g., Kauffmann et al. 2003a,b; Baldry et al. 2004; Brinchmann et al. 2004; Gallazzi et al. 2005; Mateus et al. 2006, 2007). The difference in the values obtained for the red galaxies and the red ELGs is negligible, as well as the difference between blue galaxies and blue ELGs.

The star-forming main sequence (Noeske et al. 2007) is a relation between the SFR and the stellar mass of galaxies in the form of a power law (see e.g., Elbaz et al. 2007; Speagle et al. 2014; Sparre et al. 2015; Cano-Díaz et al. 2016; Vilella-Rojo et al. 2021). The work by Nantais et al. (2020) supports that the relation remains constant with density, and Speagle et al. (2014) and Santini et al. (2017) works find no variation with redshift in the slope, but Noeske et al. (2007) find variations with redshift.

We study the main sequence of the star formation in Fig. 9. We find that blue galaxies are well placed in the main sequence. The low mass-and-high sSFR end of the main sequence is dominated by blue ELGs. This is compatible with young stars as the main mechanism of Hα emission for blue galaxies (as seen in Sect. 4.3). Meanwhile, red ELGs are mainly found in the low sSFR region, so their Hα emission is probably due to other mechanism, such as the presence of an AGN. We fit a main sequence of the star formation using the SF galaxies. The obtained fit (see black dashed line in Fig. 9) is:

$$\log \mathrm{sSFR} = (-0.43 \pm 0.07)\log M_\star + (3.78 \pm 0.64). \qquad (5)$$

Translating this fit to SFR instead of sSFR, the obtained slope is 0.57. These results are lower than the ones obtained by Martínez-Solaeche et al. (2022) analysing the whole AEGIS field. In that work, they calculate the SFR through the Hα flux and the SFH provided by `BaySeAGal`. The values of the slope (in the SFR versus mass fit) are both higher than our results. This means that sSFR decreases more rapidly with mass for the galaxies in this cluster than for galaxies in lower density environments, which is the dominant population in AEGIS (González Delgado et al. 2022). However, the SF galaxies with $\log M_\star < 9.8\,M_\odot$ shows a flatter slope that would

---

[6] In this text, sSFR is expressed in units of Gyr^{-1}; and log sSFR is the decimal logarithm of the sSFR.
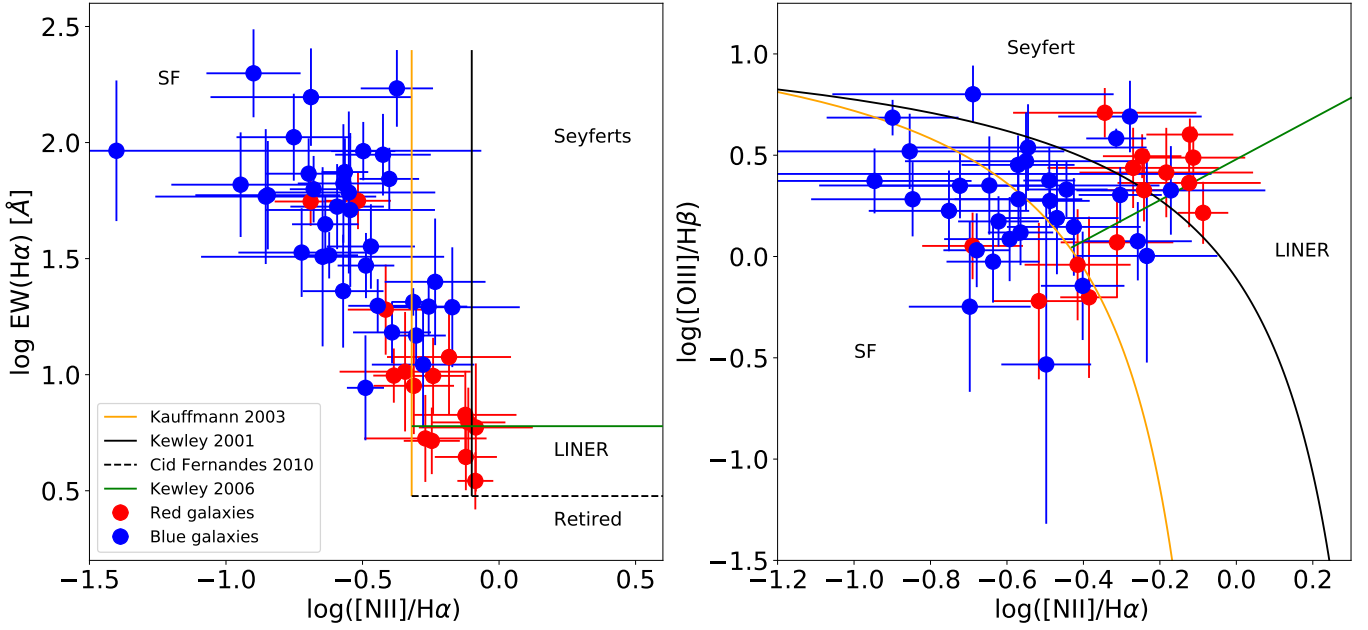
Fig. 8. ELG classification diagrams. *Left panel*: WHAN diagram with the galaxies classified as emission line galaxies. Red points represent red galaxies and blue points, blue galaxies. The solid orange and black lines represent the Cid Fernandes et al. (2010) transposition of the Kauffmann et al. (2003a) and Kewley et al. (2001) SF-AGN distiction criteria, and the green solid line represents the transposition of the Kewley et al. (2006) made by Cid Fernandes et al. (2010). The dashed black line represents the distinction between retired galaxies and LINERs (Cid Fernandes et al. 2011). *Right panel*: BPT diagram for the emission line galaxy population. The colour coding is the same as the left panel.
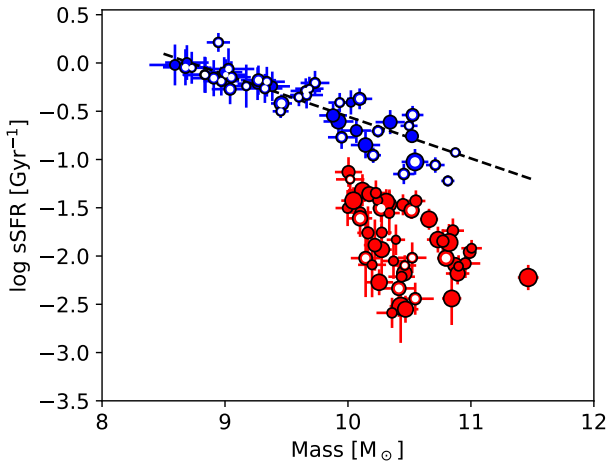
Fig. 9. Star formation main sequence. Red dots represent the red galaxies. Blue dots represent blue galaxies. White dots represent the ELG population (selected in Sect. 3.3) with inferred EW(Hα) > 6 Å. Dot size is proportional to the inverse distance to the BCG.

suggest that the sSFR is almost independent of the mass. This also holds true for the results from other works, such as Boogaard et al. (2018), Vilella-Rojo et al. (2021), Puertas et al. (2017), Renzini & Peng (2015), Zahid et al. (2012), Shin et al. (2021), Belfiore et al. (2016), Cano-Díaz et al. (2016, 2019), and Sánchez et al. (2018).

5. Discussion

The spatial distribution of the galaxy populations and the variation of galaxy properties with the cluster-centric radius is a key piece of information in improving our understanding of the

role of environment for quenching the star formation in galaxies (Donnari et al. 2021; Dacunha et al. 2022; Niemiec et al. 2022), Galaxy-galaxy or galaxy-ICM interactions are more efficient at the cluster centre, where the density of galaxies and the density of the gas are higher. Therefore, it is expected that environmental processes are more efficient inside the virial radius (Alonso et al. 2012; Raj et al. 2019). However, other processes, such as galaxy harassment, ram-pressure stripping, and starvation can act outside the virialised region, being also effective at the cluster periphery (Bahé et al. 2013; Zinger et al. 2018; Lacerna et al. 2022). The analysis of the galaxy populations, SFR and SFH have been proven to be very useful to study quenching and cluster formation scenarios (see e.g., von der Linden et al. 2010).

In this section we discuss the distribution of the galaxy populations within the cluster. The fraction of red, blue, and star-forming galaxies as well as AGN as a function of the radial distance to the cluster centre provide clues about the relevance of the environment and AGN feedback in the quenching of star formation. We also study the variation of the SFH parameters of galaxies that are in the central part ($r \leq 0.5R_{200}$), with respect to outskirt regions ($r > 0.5R_{200}$); thus, the SFH-distance relation provides information about the accretion history and the differential quenching time scales. We finish the discussion with the variation of stellar population properties with cluster-centric radius; in particular, the sSFR-distance relation traces how the environment-quenching process proceeds.

5.1. Spatial distribution of the galaxy populations

The 2D map distribution of the galaxy populations of the cluster is shown in Fig. 10. Most of the red galaxies are located inside the inner region ($d < 0.5R_{200}$ from the BCG), while half of the blue galaxies are located around 0.9 R_{200}. This visual inspection is corroborated by the mean distance of the RG, which is $0.60R_{200}$, while for BG is around $0.98R_{200}$, which is almost the
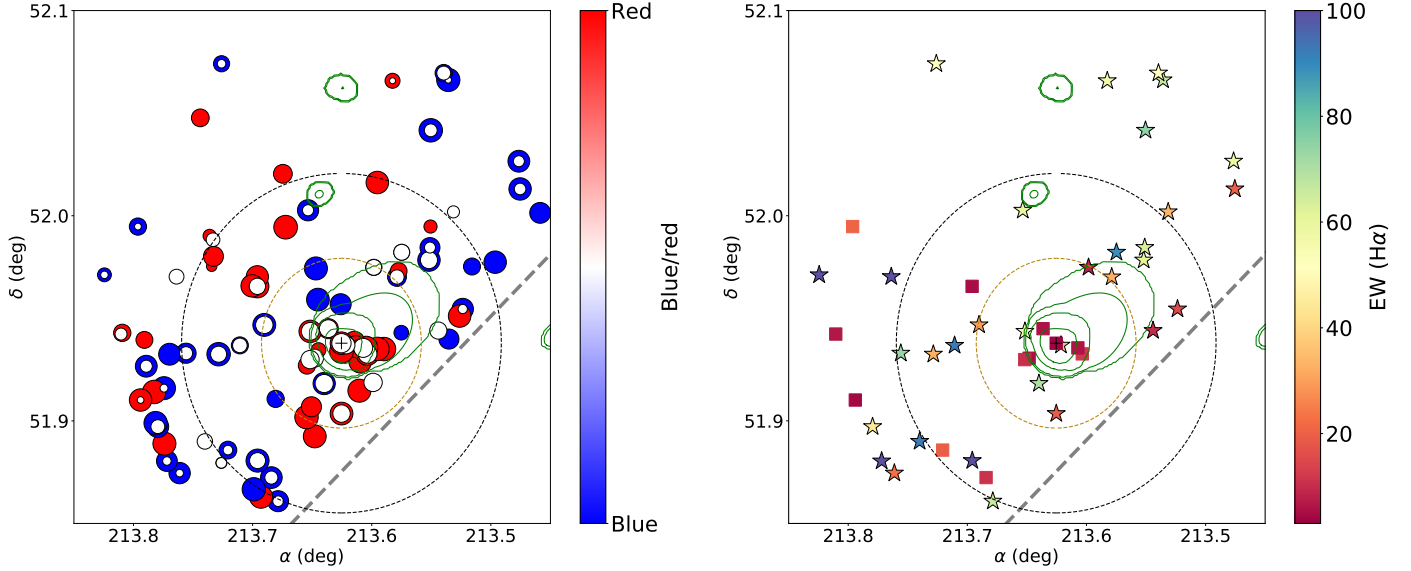
Fig. 10. Spatial distribution of the galaxy populations in the cluster. *Left panel*: spatial distribution of the red, blue, and emission line galaxy populations. Blue dots represent blue galaxies. Red galaxies are represented with red dots. White dots over red and blue dots represent the ELG. Dot size is proportional to the AMICO association probability. The dashed golden and black circles represents the $0.5R_{200}$ and R_{200} distances to the BCG, respectively. The grey dashed line represents the limit of the FoV of miniJPAS. The black cross represents the position of the BCG. Green contours represent the X-ray emission in the 0.5–2 keV energy band from XMM data (Bonoli et al. 2021). Energy levels are 3.654×10^{-16}, 1.218×10^{-15}, 3.654×10^{-15} and 1.218×10^{-14} ergs s^{-1} cm^{-2} arcmin^{-2}. *Rigt panel*: spatial distribution of the SF and AGN. Stars represent SF galaxies and squares the AGNs. The color code represent the inferred EW(Hα). The rest of the symbols are the same as in the left panel.
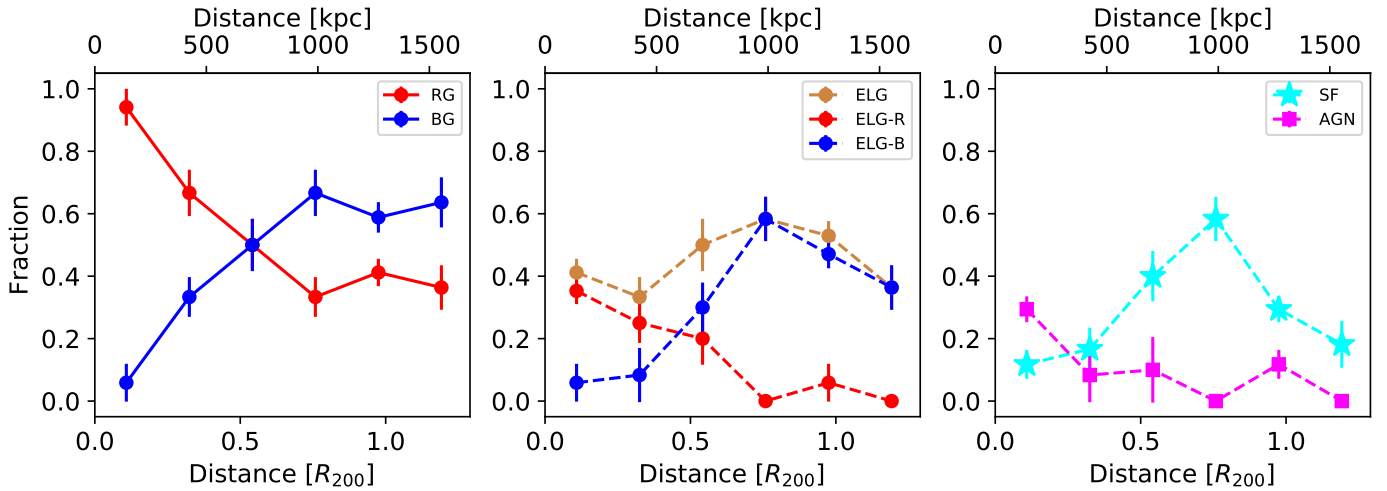
Fig. 11. Radial variation of the galaxy populations in the cluster. *First panel*: radial variation of the fraction of red and blue galaxies. Red points represent the fraction of red galaxies, blue points represent the fraction of blue galaxies. *Second panel*: fraction of ELG, red ELG, and blue ELG as a function of distance. Peru points are the total fraction of ELG, red points are the fraction of red ELG, and blue points are the fraction of blue ELG. *Third panel*: fraction of SF galaxies and AGNs as a function of the distance to the BCG. Cyan stars represent the fraction of star-forming galaxies. Magenta squares represent the fraction of AGN.

same as the mean distance of ELGs ($0.90R_{200}$, $0.98R_{200}$ for the SF galaxies, and $0.64R_{200}$ for the AGNs). Moreover, the distribution of the ELGs is very similar to that of BGs, because most of the ELGs are BGs. This indicates that RGs are more prominent in denser environments than BGs, as seen in previous works (see e.g., Balogh et al. 2004). Also, ELGs appear to show a more uniform distance distribution, which is in accordance with the results of the literature, such as Haines et al. (2012, 2015), Noble et al. (2013, 2016), Mercurio et al. (2021). However, our ELG population is not composed exclusively of SF galaxies, as there are also AGN candidates; this is justified by the presence of ELGs in denser environments. In fact, most of the AGNs are

located in the central region, while the number of SF galaxies increases with distance.

To quantify the spatial variation of the galaxy populations, we discuss how the fraction of the different galaxy populations changes with the distance to the BCG (see Fig. 11). Red galaxies clearly dominate over blue galaxies in the inner regions (up to $d \sim 0.5R_{200}$). At this point, we are not affected by the incompleteness of the observations. The fraction of red galaxies steeply decreases, as the fraction of blue galaxies increases with the distance, but the fraction of red galaxies remains above the value obtained by González Delgado et al. (2021) even at distances larger than R_{200}. It is also interesting to note that the

fraction of red galaxies is equal to the fraction of blue galaxies at $d \approx 0.5R_{200}$. Thus, we can conclude that inside the virialised region, the red galaxy population dominates over the blue one.

The fraction of ELG slightly increases with distance, up to $d \approx R_{200}$ and then decreases again. This decrease of the ELG fraction for $d > R_{200}$ could be a consequence of the possible observational incompleteness of our sample at larger distances. The fraction remains below 0.6 at all distances. This fraction is below the ~80% star-forming field AEGIS population at $z = 0.2-0.3$ (Martínez-Solaeche et al. 2022). If we separate blue and red ELG, we find that most of the ELG are red in the inner areas, but their fraction rapidly decreases and is negligible at distances larger than $d \approx 0.5R_{200}$. In contrast, the fraction of blue ELG is negligible inside $d \approx 0.3R_{200}$, and then increases steeply. An almost equal behaviour is found for AGN and SF galaxy populations, respectively. As it happens for the blue ELG, the fraction of SF galaxies increases up to 0.6 as the distance increases. Although it decreases to lower values at distances higher than $d \approx 0.8R_{200}$. This may be due to our incompleteness in the observations or to the presence of composite blue galaxies that cannot be clearly classified neither as SF nor as AGN.

Thus, blue and star-forming galaxies are more common beyond the cluster virialised region, in agreement with other works, such as Haines et al. (2012, 2015), Noble et al. (2013, 2016), Mercurio et al. (2021). As reported by Olave-Rojas et al. (2018), we find that the fraction of red galaxies remains higher than in the field at distances larger than R_{200}. However, in contrast to Guglielmo et al. (2019), we do not find a larger fraction of SF galaxies than blue galaxies, except for the most central region, where a reactivation of the SF may be taking place, due to the aforementioned mechanisms. The radial profile of the AGN fraction could compatible with the results by Peluso et al. (2022), who find a significant abundance of AGNs in galaxies that have suffered ram-pressure stripping, taking into account the relation between ram-pressure stripping and the ICM density AGN feedback might play a role at the centre due to the increase of AGN fraction toward it; but this study could not explain the large fraction (>50%) of red galaxies within $0.5R_{200}$. Other processes related to the environment, along with possible previous mass-quenching, may be acting in the cluster.

5.2. Stellar population properties: Radial variation of the colours, mass, and ages

The variation of the abundance of red and blue galaxies has an important effect on the radial variation of the galaxy properties, particularly on the colours and ages of the stellar populations.

We studied the radial profiles of the $(u-r)_{int}$ colour, the mass density (with the area corrected from mask an incompleteness effects), and the $\langle \log age \rangle_M$ (see Fig. 12). The colour, $(u-r)_{int}$, decreases with the radial distance; however, this is in part due to the radial variation of the fraction of red and blue galaxies in the cluster. When the galaxy population is segregated in red and blue galaxies, we find that most of the red galaxies have very similar $(u-r)_{int}$, while blue galaxies become bluer going from the cluster centre and further out towards the edges This is probably associated with a change in the age of the blue galaxy population. Red galaxies ages stay approximately constant at $\langle \log age \rangle_M \approx 9.6$[7]. Meanwhile, the mean age of BGs decreases as the distance to the BCG increases by about 0.3 dex in the inner $0.5R_{200}$. The stellar mass surface density of the red galaxies decreases with the distance to the BCG, reflecting that the most massive galaxies are

sited in the inner $0.5R_{200}$. Blue galaxies show a lower mass density and a smoother slope than RGs, but they show similar stellar mass density as the red galaxies beyond $0.5R_{200}$.

Therefore, we find that red, more massive, older galaxies, are found in the inner areas while we find, blue, younger, and less massive galaxies in the outskirts. These properties are generally associated with galaxies in the red sequence (which also, show low values of star formation) and the blue cloud with usually higher levels of star formation than most galaxies in the red sequence (see e.g., Kauffmann et al. 2003a,b; Baldry et al. 2004; Brinchmann et al. 2004; Gallazzi et al. 2005; Mateus et al. 2006, 2007).

The stellar ages of the blue galaxies show a clear gradient with cluster-centric distance. However, the mean ages of the red galaxies is almost constant with the radial distance. It suggests that these galaxies were probably quenched earlier than their accretion to the cluster or during the first epoch of the accretion.

5.3. SFH: Spatial variation

We go on to investigate the spatial variation of the SFH of the cluster galaxies. Before doing that, however, we comment here on the uncertainties involved.

The reliability of our methodology has been previously assessed in González Delgado et al. (2021), where we have shown that the SFH of a complete sub-sample of miniJPAS galaxies selected at $z \sim 0.1$ constrains the cosmic evolution of the star formation rate density up to $z \sim 3$, producing results in good agreement with those derived from cosmological surveys. We have further shown that the galaxy properties (stellar mass, ages, and metallicity) can be inferred by fitting the J-spectra with the non-parametric codes MUFFIT, AlStar, and TGASPEX, and the results are similar to those obtained by BaySeAGal using the same delayed-τ model used in this work (see Table 1 in González Delgado et al. 2021).

Reassuring as these statistical results may be, we should not lose sight of the inherent difficulties in estimating SFHs of individual galaxies (e.g., Ocvirk et al. 2006). Our Bayesian analysis, based on an analytical prescription for the SFH (Eq. (1)), is just one out of a vast spectrum of alternative approaches. Parametric models such as our delayed-τ model are known to lack flexibility to emulate the diversity of SFHs in galaxies (e.g., Dressler et al. 2016; Pacifici et al. 2016) and to induce considerable biases in some cases (e.g., Lower et al. 2020). Non-parametric models alleviate these problems, but the higher dimensionality associated with the added flexibility requires extra care when specifying the priors, which may have a significant impact in the estimated properties (Leja et al. 2019). Moreover, it has been previously shown that only a few characteristic episodes in the SFH can be retrieved from the SED-fitting (Cid Fernandes et al. 2005; Ocvirk et al. 2006; Asari et al. 2007; Tojeiro et al. 2017).

Despite all the caveats involved, our previous analysis of ~8000 miniJPAS galaxies, where we detected only small differences between properties derived though parametric and non-parametric codes (significantly below the 0.4 dex in $\log M_\star$, inferred for the SED-fitting of broad band photometry of mock data of cosmological galaxy formation simulations by Lower et al. 2020) gives us confidence that we can use our results to investigate the general trend of the spatial variation of the SFH among the galaxy cluster members. The comparative and statistical nature of this analysis further alleviates worries associated with the SFH parameters derived for each galaxy; however, as discussed above, this approach should be treated with caution.

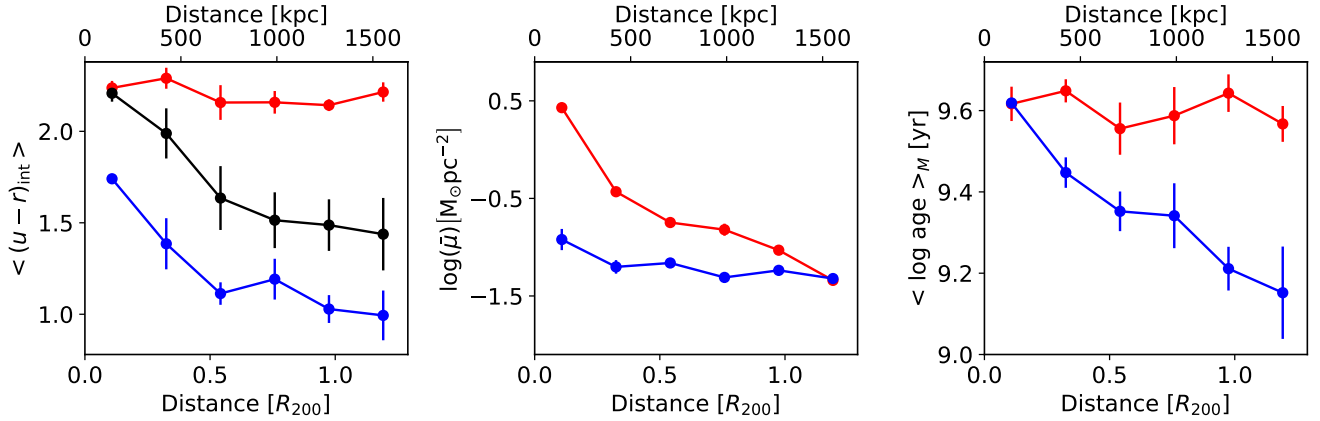[7] This is the logarithm of the stellar ages expressed in yr.

Fig. 12. Radial distribution of the stellar mass surface density, the mean mass-weighted age and the mean $(u - r)_{int}$ colour. The grey dashed lines represent the limit of the FoV of miniJPAS. Red dots represent the values for the red galaxies and blue dots represent the values for the blue galaxies. Black dots represent the values of $(u - r)_{int}$ for all the galaxies.

Table 2. Averages and dispersions for the SFH parameters.

SP	RG	BG	RG ($d < 0.5$)	BG ($d < 0.5$)	RG ($0.5 < d < 1$)	BG ($0.5 < d < 1$)	RG ($d > 1$)	BG ($d > 1$)
t_0	6.44 ± 1.76	6.00 ± 1.72	6.64 ± 1.75	7.69 ± 0.17	6.30 ± 1.86	6.37 ± 1.59	6.18 ± 1.65	5.33 ± 1.66
τ/t_0	0.12 ± 0.02	0.94 ± 0.63	0.12 ± 0.03	0.46 ± 0.21	0.12 ± 0.02	0.83 ± 0.49	0.11 ± 0.02	1.14 ± 0.70

Notes. Values are the mean and standard deviation of the red and blue galaxy members, and for galaxies inside $0.5R_{200}$, between $0.5R_{200}$ and R_{200} and outside R_{200}.

We focus on two parameters for this study: t_0, the lookback time when the star formation began, and τ/t_0, a measure of the extent of the star formation that is better constrained than t_0 or τ. Table 2 and Fig. 13 summarise our results. We divide the galaxies into blue and red ones once again. We further divide galaxies by their (projected) distances to the BCG into smaller than $0.5R_{200}$, between $0.5R_{200}$ and $1R_{200}$, and larger than R_{200} bins. This allows us to distinguish the effect of the environment in the SFH for the central virialised area and the outer regions.

The parameter t_0 shows similar values for red and blue galaxies at all distances. This would suggest that most galaxies started forming stars roughly at the same epoch (around ~6.5 Gyr). The main differences appear in the blue galaxies within and outside of $0.5R_{200}$. Blue galaxies in the inner region show the highest mean value of t_0, but they are very few and this value is compatible with the one obtained for red galaxies at similar distances. Blue galaxies in the outer region ($d > R_{200}$) show a lower value for t_0. This could be a consequence of these galaxies being in the cluster infall region (Rines & Diaferio 2006).

Since values of t_0 are very similar for most galaxies all over the cluster, we interpret the low values of τ/t_0 as short episodes of star formation and large values of this parameter as star formation processes that are more extended over time. Red galaxy values of $\tau/t_0 \sim 0.12$, no matter their distance to the BCG, suggest that their star formation was shut down very fast. On the contrary, blue galaxies show larger values of this fraction than red galaxies at all distances and there is a clear increase in τ/t_0 as the distance to the BCG increases.

Thus, these results suggest a faster quenching process for blue galaxies in the dense (inner) regions; while red galaxies might be quenched earlier on and independently of the distance to the cluster centre in an earlier cluster accretion epoch. Moreover, the quenching of the star formation of red galaxies might be linked to the AGN or galaxy stellar mass, rather than to the environment because at the smaller cluster-centric distance is where

we find the most massive galaxies and the fraction of AGN is larger.

5.4. sSFR: Radial variation

From the SFH parameters, we can conclude that red galaxies have already been quenched independently of their position in the cluster; whereas for blue galaxies, the quenching process proceeds from the inner to the outer regions of the cluster. To confirm this conclusion, we study the variation of the sSFR with the distance (see Fig. 14). It is worth noticing that blue galaxies have a sSFR at all the cluster-centric radius that are above sSFR $= 0.1\,\mathrm{Gyr}^{-1}$, which is the threshold adopted by Peng et al. (2010) to differentiate star-forming galaxies from quenched galaxies. The mean sSFR of blue galaxies also clearly increases from inside-out of the cluster; in contrast, the mean sSFR of the red galaxies remains constant within the error bars. This suggests that red galaxies have quenched before their accretion to the cluster or were quenched within it in an earlier accretion epoch, while blue galaxies are still in the process of quenching. This could be related to the pre-processing effects during the infalling processes (assuming galaxies are incorporated in substructures already evolving; see e.g., Gavazzi et al. 2003; Aguerri et al. 2017; Donnari et al. 2021). Our results are differ from those of Knowles et al. (2022), who find no dependence of the star formation with the cluster-centric distance – but the distinction between red and blue galaxies is key for this result. In particular, the results of Balogh et al. (1999; in a redshift range similar to our cluster) show that the last episode of star formation is more recent for galaxies in the outskirts than in inner regions.

5.5. On the pre-processing scenario

To sum up, all the galaxies were formed around the same epoch (with the exception of some outer blue ones). Red galaxies had
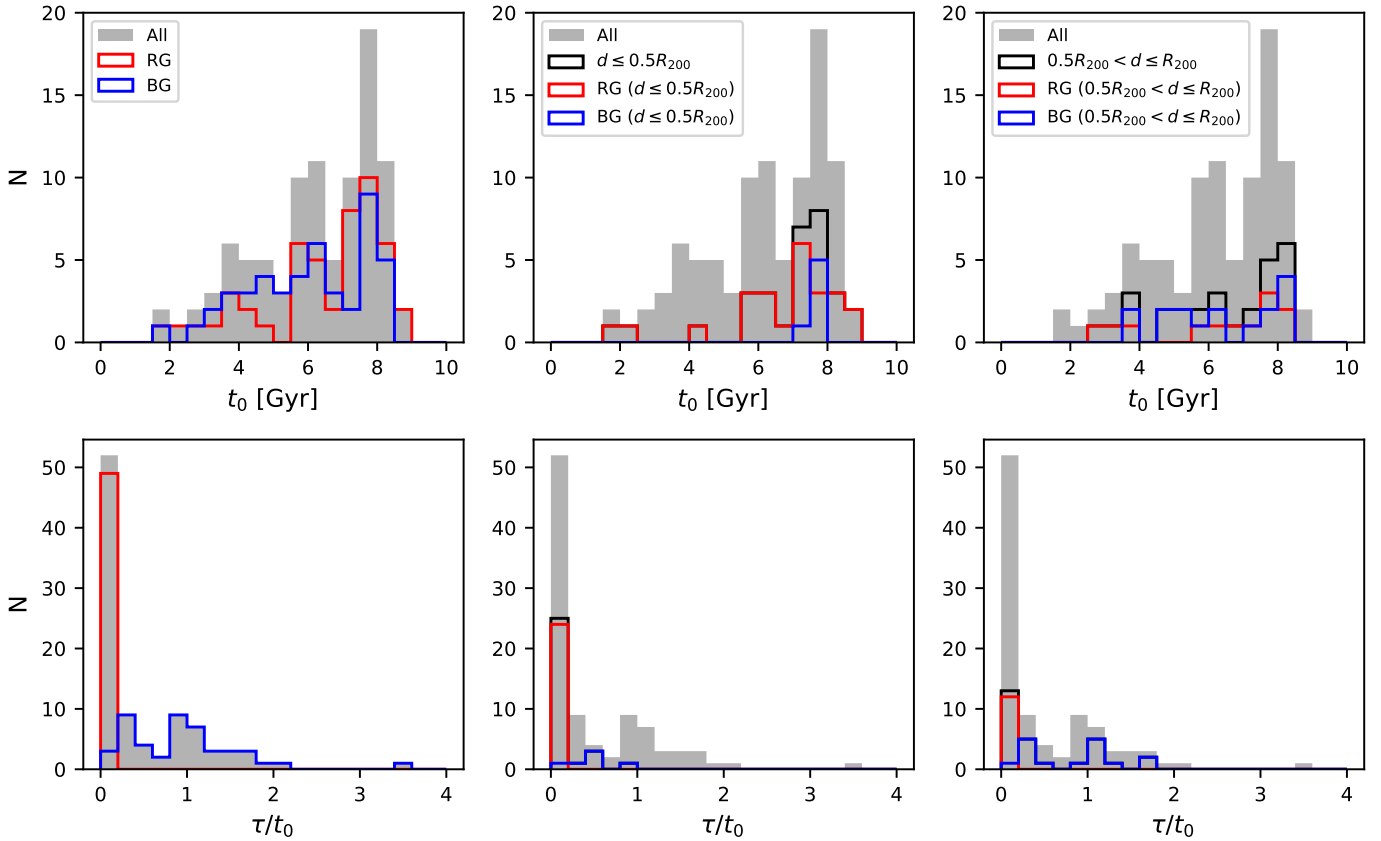
Fig. 13. Distributions of SFH parameters t0 (*top row*) and $\tau/t0$ (*bottom row*), shown from left to right. Grey histograms represent the distribution of all the galaxies in the cluster in all panels. Red, blue, and black histograms represent the distribution of red, blue and all galaxies at different cluster-centric distances: all the galaxies in the cluster (first column), galaxies within $0.5R_{200}$ (second column), and galaxies within $0.5R_{200}$ and R_{200} (third column).

shorter star formation periods and have a similar SFH, independently of their position in the cluster. Meanwhile, blue galaxies are still forming stars or have been forming them until very recently, and galaxies in the inner regions are quenching faster than in the outer ones. However, red galaxies were quenched earlier on, independently of their position on the cluster. These results suggest different evolutionary paths and accretion histories for red and blue galaxies.

Illustris cosmological simulations have shown that pre-processing plays a relevant role in quenching galaxies (Donnari et al. 2021). They find that satellites can be quenched before infalling in dense environment, or after being accreted into any host; or while being members of pre-processing hosts other than the actual one where they are found today. AGN feedback and mass-quenching may be acting in the pre-processing host phases. This is a possible scenario for explaining the spatial variation of the SFH of red and blue galaxies, their abundance, AGN fraction, and variation of the galaxies properties with the radial distance to the cluster centre.

Another scenario is the 'slow-then-rapid' quenching (see e.g., Maier et al. 2019; Roberts et al. 2019; Kipper et al. 2021), whereby galaxies undergo slow quenching processes and, once they enter a dense environment, start a faster quenching phase. Results from Pallero et al. (2022), using the C-EAGLE simulation support this scenario. They show that these processes usually become relevant at $\sim R_{200}$, where the ICM reaches a density high enough for ram-pressure stripping to become relevant. They also

find that the fraction of galaxies quenched in situ, in comparison the fraction of galaxies quenched because of pre-processing, decreases as M_{200} increases.

A combination of both scenarios may serve us to interpret the spatial and radial distributions of the stellar population properties that are found. We identified red galaxies with very similar properties along the whole cluster. Red galaxies may quenched within smaller structures that were later accreted to the cluster. According to the results from Pallero et al. (2022) , for a cluster of this mass ($M_{200} = 3.3 \times 10^{14} \, M_\odot$), we would expect a similar fraction of galaxies quenched inside the cluster and quenched via pre-processing. However, we find that ~73% of the red galaxies are within R_{200}, so in order to be compatible with these results, some of the inner red galaxies would have to be part of a different halo. On the other hand, the results from Donnari et al. (2021) show that the pre-processing scenario is relevant for low mass galaxies and that massive galaxies quench on their own.

If we assume that some of the blue galaxies belong to the original halo and some have been accreted later, we could explain the behaviour of blue galaxies and the greater dispersion of their properties, as well as the greater amount of quenching among inner ones. However, Pallero et al. (2022) estimate that the quenching timescale for galaxies once the in-fall beyond R_{200} is ~1 Gyr, but our estimations of Δt_q are larger for blue galaxies, and only some of the red galaxies are compatible with these values, regardless of their distance to the cluster centre. These
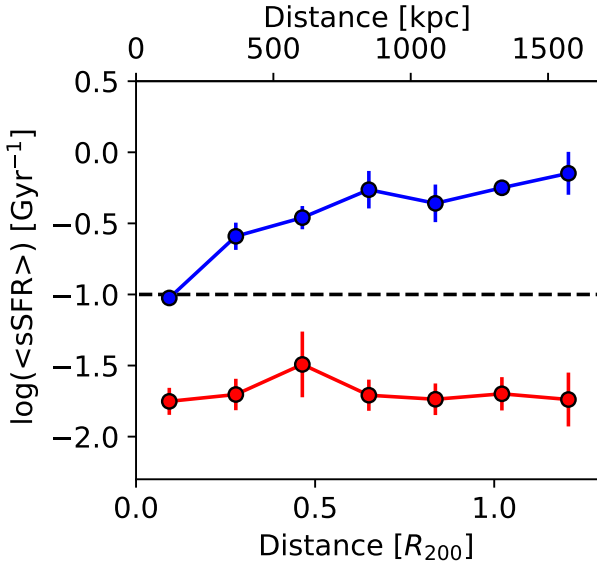
Fig. 14. Radial distribution of the mean sSFR. The gray dashed lines shows the limit of the FoV of miniJPAS. The black dashed line shows Peng et al. (2010) criteria to distinguish among star-forming and quiescent galaxies. Red dots represent red galaxies. Blue dots represent blue galaxies.

suggest that the accretion and evolution scenario may be more complex and a different model is required.

6. Summary and conclusions

In this paper, we study the stellar population properties of the miniJPAS cluster mJPC2470-1771 using the J-PAS photometric filter system. Its redshift is $z = 0.29$, its mass $M_{200} = 3.3 \times 10^{14} M_{\odot}$, and its radius $R_{200} = 1.304$ kpc. We used the fossil record method for stellar populations and we analysed the SEDs (J-spectra) of the galaxy members of the cluster. The cluster was detected and its members were selected using AMICO (Maturi et al., in prep.) based on PHOTOZ, with an ultimate selection of 99 objects.

We used the BaySeAGal code to fit the stellar continuum and constrain the stellar population properties by assuming a delayed-τ model for the SFH. The parameters obtained with BaySeAGal are the stellar mass, the metallicity, and the extinction A_V, t_0, and τ. We used these parameters and fittings to calculate the mass- and light-weighted ages and the extinction-corrected rest frame $(u - r)$ colours. We established a set of criteria to select the ELG population, using the median error of the closest filters to Hα wavelength and the predictions for the EW(Hα), EW([NII]), EW(Hβ), and EW([OIII]) made with Martínez-Solaeche et al. (2021) ANN. We used the WHAN and BPT diagrams to separate SF, AGNs, and quiescent-retired galaxies. We studied the spatial distribution of the stellar population properties in the cluster as well as the radial distribution of the abundances of red, blue, SF galaxies, and AGN hosts. The main conclusions of our analysis are as follows:

- We observe a fraction of red galaxies (52%) that is larger than that in the whole AEGIS field set of galaxies with redshift $0.25 < z < 0.35$, which is ~20%. The distribution of the stellar population properties in the mass-colour diagrams is the same as the whole set.

- We selected a total of 48 ELG. These are dominated by young galaxies and most of the blue, less massive galaxies have been selected as ELGs. There are red galaxies in this set, showing the lowest inferred values of EW(Hα), being the median value equal to 8.96 Å. 65.3% of these galaxies are probably star-forming galaxies, while 24.4% could be AGNs and the rest could be SF, AGNs, or composite galaxies.

- The red, older, more massive galaxies are mainly located in the inner part ($d < 0.5R_{200}$) of the cluster, where the density is higher. The blue, and SF galaxies are more numerous at ($d > 0.5R_{200}$), and their abundance increases with radial distance, being equal to the red galaxy fraction at $d \sim 0.5R_{200}$. The abundance of the AGNs population decreases with the radial distance and it is higher at the cluster centre.

- In analysing the SFH, we find that galaxy members were formed roughly at the same epoch, but blue galaxies have experienced more recent star formation periods. Our results are compatible with a scenario where red galaxies are quenched prior to the cluster accretion or an earlier cluster accretion epoch; whereas blue galaxies may be in the transition to be quenched. This is also supported by the radial distribution of the red and blue galaxy populations, because the mean stellar age remains constant for red galaxies, but decreases for blue galaxies along with the distance to the BCG.

- The sSFR of the red galaxies is almost constant with radial distance at sSFR ~ 0.02 Gyr^{-1}. The sSFR of blue galaxies decreases with the cluster-centric radius from sSFR ~ 0.1 Gyr^{-1} to above ~ 0.7 Gyr^{-1} beyond $0.5R_{200}$. This suggests that the quenching of blue galaxies is progressing from the inside-out of the cluster. AGN feedback or mass (or both) might also be intervening in the quenching of red galaxies.

Our results show that the environment plays a relevant role in galaxy evolution, mainly manifested through a larger fraction of red, more massive galaxies in denser regions, as well as larger fraction of AGN hosts, lower, SFRs, and shorter star formation episodes, compared to less dense regions. This also shows the power of J-PAS in studies of the role of the environment in galaxy evolution. We developed a methodology that will be transferable to J-PAS data, providing more solid results regarding the relation between galaxy evolution and the environment.

References

Aguerri, J. A. L., Agulli, I., Diaferio, A., & Dalla Vecchia, C. 2017, MNRAS, 468, 364

Alatalo, K., Appleton, P. N., Lisenfeld, U., et al. 2015, ApJ, 812, 117

Alonso, S., Mesa, V., Padilla, N., & Lambas, D. G. 2012, A&A, 539, A46

Arcila-Osejo, L., Sawicki, M., Arnouts, S., et al. 2019, MNRAS, 486, 4880

Asari, N. V., Cid Fernandes, R., Stasińska, G., et al. 2007, MNRAS, 381, 263

Ascaso, B., Benítez, N., Fernández-Soto, A., et al. 2015, MNRAS, 452, 549

Bahé, Y. M., McCarthy, I. G., Balogh, M. L., & Font, A. S. 2013, MNRAS, 430, 3017

Baldry, I. K., Glazebrook, K., Brinkmann, J., et al. 2004, ApJ, 600, 681

Baldry, I. K., Balogh, M. L., Bower, R. G., et al. 2006, MNRAS, 373, 469

Baldwin, J. A., Phillips, M. M., & Terlevich, R. 1981, PASP, 93, 5

Balogh, M. L., Morris, S. L., Yee, H. K. C., Carlberg, R. G., & Ellingson, E. 1999, ApJ, 527, 54

Balogh, M. L., Navarro, J. F., & Morris, S. L. 2000, ApJ, 540, 113

Balogh, M. L., Baldry, I. K., Nichol, R., et al. 2004, ApJ, 615, L101

Beers, T. C., Flynn, K., & Gebhardt, K. 1990, AJ, 100, 32

Belfiore, F., Maiolino, R., Maraston, C., et al. 2016, MNRAS, 461, 3111

Bellagamba, F., Maturi, M., Hamana, T., et al. 2011, MNRAS, 413, 1145

Bellagamba, F., Roncarelli, M., Maturi, M., & Moscardini, L. 2018a, MNRAS, 473, 5221

Bellagamba, F., Roncarelli, M., Maturi, M., & Moscardini, L. 2018b, MNRAS, 473, 5221

Benítez, N., Dupke, R., Moles, M., et al. 2014, ArXiv e-prints [arXiv:1403.5237]

Benítez, N., Gaztañaga, E., Miquel, R., et al. 2009, ApJ, 691, 241

Bernardi, M., Nichol, R. C., Sheth, R. K., Miller, C. J., & Brinkmann, J. 2006, AJ, 131, 1288

Berrier, J. C., Stewart, K. R., Bullock, J. S., et al. 2009, ApJ, 690, 1292

Bertin, E., & Arnouts, S. 1996, A&AS, 117, 393

Bluck, A. F. L., Mendel, J. T., Ellison, S. L., et al. 2014, MNRAS, 441, 599

Bluck, A. F. L., Maiolino, R., Piotrowska, J. M., et al. 2020, MNRAS, 499, 230

Bonoli, S., Marín-Franch, A., Varela, J., et al. 2021, A&A, 653, A31

Boogaard, L. A., Brinchmann, J., Bouché, N., et al. 2018, A&A, 619, A27

Boselli, A., & Gavazzi, G. 2006, PASP, 118, 517

Boselli, A., Boissier, S., Cortese, L., & Gavazzi, G. 2008, ApJ, 674, 742

Boselli, A., Lupi, A., Epinat, B., et al. 2021, A&A, 646, A139

Bower, R. G., Ellis, R. S., Rose, J. A., & Sharples, R. M. 1990, AJ, 99, 530

Boylan-Kolchin, M., Springel, V., White, S. D. M., Jenkins, A., & Lemson, G. 2009, MNRAS, 398, 1150

Brinchmann, J., Charlot, S., White, S. D. M., et al. 2004, MNRAS, 351, 1151

Brownson, S., Bluck, A. F. L., Maiolino, R., & Jones, G. C. 2022, MNRAS, 511, 1913

Bruzual, G., & Charlot, S. 2003, MNRAS, 344, 1000

Bundy, K., Bershady, M. A., Law, D. R., et al. 2015, ApJ, 798, 7

Butcher, H., & Oemler, A. J. 1978, ApJ, 219, 18

Butcher, H., & Oemler, A. J. 1984, ApJ, 285, 426

Calzetti, D., Armus, L., Bohlin, R. C., et al. 2000, ApJ, 533, 682

Cano-Díaz, M., Sánchez, S. F., Zibetti, S., et al. 2016, ApJ, 821, L26

Cano-Díaz, M., Ávila-Reese, V., Sánchez, S., et al. 2019, MNRAS, 488, 3929

Cappellari, M., Emsellem, E., KrAJnović, D., et al. 2011, MNRAS, 413, 813

Catalán-Torrecilla, C., Gil de Paz, A., Castillo-Morales, A., et al. 2015, A&A, 584, A87

Cenarro, A. J., Moles, M., Marín-Franch, A., et al. 2014, SPIE Conf. Ser., 9149, 91491I

Cenarro, A. J., Ederoclite, A., Iñiguez, C., et al. 2018, SPIE Conf. Ser., 10700, 107000D

Chabrier, G. 2003, PASP, 115, 763

Charlot, S., & Fall, S. M. 2000, ApJ, 539, 718

Chies-Santos, A. L., Rodríguez del Pino, B., Aragón-Salamanca, A., et al. 2015, MNRAS, 450, 4458

Cid Fernandes, R., Mateus, A., Sodré, L., Stasińska, G., & Gomes, J. M. 2005, MNRAS, 358, 363

Cid Fernandes, R., Stasińska, G., Schlickmann, M. S., et al. 2010, MNRAS, 403, 1036

Cid Fernandes, R., Stasińska, G., Mateus, A., & Vale Asari, N. 2011, MNRAS, 413, 1687

Civera, T., & Hernández, J. 2020, ASP Conf. Ser., 527, 101

Clemens, M. S., Bressan, A., Nikolic, B., et al. 2006, MNRAS, 370, 702

Contini, E., Gu, Q., Ge, X., et al. 2020, ApJ, 889, 156

Cooper, M. C., Gallazzi, A., Newman, J. A., & Yan, R. 2010, MNRAS, 402, 1942

Cristóbal-Hornillos, D., Varela, J., Ederoclite, A., et al. 2014, SPIE Conf. Ser., 9152, 91520O

Dacunha, T., Belyakov, M., Adhikari, S., et al. 2022, MNRAS, 512, 4378

Davies, L. J. M., Robotham, A. S. G., Driver, S. P., et al. 2015, MNRAS, 452, 616

Davis, M., Guhathakurta, P., Konidaris, N. P., et al. 2007, ApJ, 660, L1

De Rijcke, S., Van Hese, E., & Buyle, P. 2010, ApJ, 724, L171

Dekel, A., & Birnboim, Y. 2006, MNRAS, 368, 2

Di Matteo, T., Springel, V., & Hernquist, L. 2005, Nature, 433, 604

Diaferio, A., Kauffmann, G., Balogh, M. L., et al. 2001, MNRAS, 323, 999

Díaz-García, L. A., Cenarro, A. J., López-Sanjuan, C., et al. 2019, A&A, 631, A156

Donnari, M., Pillepich, A., Joshi, G. D., et al. 2021, MNRAS, 500, 4004

Dressler, A. 1980, ApJ, 236, 351

Dressler, A., Kelson, D. D., Abramson, L. E., et al. 2016, ApJ, 833, 251

Elbaz, D., Daddi, E., Le Borgne, D., et al. 2007, A&A, 468, 33

Ellingson, E., Lin, H., Yee, H. K. C., & Carlberg, R. G. 2001, ApJ, 547, 609

Ellison, S. L., Mendel, J. T., Patton, D. R., & Scudder, J. M. 2013, MNRAS, 435, 3627

Esposito, F., Vallini, L., Pozzi, F., et al. 2022, MNRAS, 512, 686

Fabian, A. C. 2012, ARA&A, 50, 455

Fogarty, L. M. R., Scott, N., Owers, M. S., et al. 2014, MNRAS, 443, 485

Fumagalli, M., Patel, S. G., Franx, M., et al. 2012, ApJ, 757, L22

Gallazzi, A., Charlot, S., Brinchmann, J., White, S. D. M., & Tremonti, C. A. 2005, MNRAS, 362, 41

Gao, L., Navarro, J. F., Frenk, C. S., et al. 2012, MNRAS, 425, 2169

Garn, T., Sobral, D., Best, P. N., et al. 2010, MNRAS, 402, 2017

Gavazzi, G., Cortese, L., Boselli, A., et al. 2003, ApJ, 597, 210

Gómez, P. L., Nichol, R. C., Miller, C. J., et al. 2003, ApJ, 584, 210

Gonzalez Delgado, R. M., Perez, E., Tenorio-Tagle, G., et al. 1994, ApJ, 437, 239

González Delgado, R. M., Díaz-García, L. A., de Amorim, A., et al. 2021, A&A, 649, A79

González Delgado, R. M., Rodríguez-Martín, J. E., Díaz-García, L. A., et al. 2022, A&A, 666, A84

Guglielmo, V., Poggianti, B. M., Vulcani, B., et al. 2019, A&A, 625, A112

Gunn, J. E., Gott, J., & Richard, I. 1972, ApJ, 176, 1

Guo, Y., Carleton, T., Bell, E. F., et al. 2021, ApJ, 914, 7

Haines, C. P., Pereira, M. J., Sanderson, A. J. R., et al. 2012, ApJ, 754, 97

Haines, C. P., Pereira, M. J., Smith, G. P., et al. 2015, ApJ, 806, 101

Haines, C. P., Iovino, A., Krywult, J., et al. 2017, A&A, 605, A4

Hayashi, M., Shimakawa, R., Tanaka, M., et al. 2020, PASJ, 72, 86

Hernán-Caballero, A., Varela, J., López-Sanjuan, C., et al. 2021, A&A, 654, A101

Hook, I. M., Jørgensen, I., Allington-Smith, J. R., et al. 2004, PASP, 116, 425

Iglesias-Páramo, J., Arroyo, A., Kehrig, C., et al. 2022, A&A, 665, A95

Janz, J., Salo, H., Su, A. H., & Venhola, A. 2021, A&A, 647, A80

Jian, H.-Y., Lin, L., Oguri, M., et al. 2018, PASJ, 70, S23

Joseph, R. D., & Wright, G. S. 1985, MNRAS, 214, 87

Joshi, B. A., Appleton, P. N., Blanc, G. A., et al. 2019, ApJ, 878, 161

Joshi, G. D., Pillepich, A., Nelson, D., et al. 2020, MNRAS, 496, 2673

Kauffmann, G., Heckman, T. M., White, S. D. M., et al. 2003a, MNRAS, 341, 54

Kauffmann, G., Heckman, T. M., White, S. D. M., et al. 2003b, MNRAS, 341, 33

Kauffmann, G., Heckman, T. M., Tremonti, C., et al. 2003a, MNRAS, 346, 1055

Kauffmann, G., White, S. D. M., Heckman, T. M., et al. 2004, MNRAS, 353, 713

Kennicutt, R. C. Jr 1998, ARA&A, 36, 189

Kennicutt, R. C., & Evans, N. J. 2012, ARA&A, 50, 531

Kewley, L. J., Dopita, M. A., Sutherland, R. S., Heisler, C. A., & Trevena, J. 2001, ApJ, 556, 121

Kewley, L. J., Geller, M. J., Jansen, R. A., & Dopita, M. A. 2002, AJ, 124, 3135

Kewley, L. J., Groves, B., Kauffmann, G., & Heckman, T. 2006, MNRAS, 372, 961

Khostovan, A. A., Malhotra, S., Rhoads, J. E., et al. 2021, MNRAS, 503, 5115

Kipper, R., Tamm, A., Tempel, E., de Propris, R., & Ganeshaiah Veena, P. 2021, A&A, 647, A32

Knowles, K., Cotton, W. D., Rudnick, L., et al. 2022, A&A, 657, A56

Kodama, T., Balogh, M. L., Smail, I., Bower, R. G., & Nakata, F. 2004, MNRAS, 354, 1103

Koester, B. P., McKay, T. A., Annis, J., et al. 2007, ApJ, 660, 239

Koyama, Y., Hayashi, M., Tanaka, M., et al. 2018, PASJ, 70, S21

Lacerna, I., Rodriguez, F., Montero-Dorta, A. D., et al. 2022, MNRAS, 513, 2271

Leja, J., Carnall, A. C., Johnson, B. D., Conroy, C., & Speagle, J. S. 2019, ApJ, 876, 3

Lewis, I., Balogh, M., De Propris, R., et al. 2002, MNRAS, 334, 673

Lin, Y.-T., Hsieh, B.-C., Lin, S.-C., et al. 2017, ApJ, 851, 139

Lisenfeld, U., Alatalo, K., Zucker, C., et al. 2017, A&A, 607, A110

Lizée, T., Vollmer, B., Braine, J., & Nehlig, F. 2021, A&A, 645, A111

López Fernández, R., González Delgado, R. M., Pérez, E., et al. 2018, A&A, 615, A27

López-Sanjuan, C., Varela, J., Cristóbal-Hornillos, D., et al. 2019, A&A, 631, A119

Lower, S., Narayanan, D., Leja, J., et al. 2020, ApJ, 904, 33

Maier, C., Ziegler, B. L., Haines, C. P., & Smith, G. P. 2019, A&A, 621, A131

Malumuth, E. M., & Richstone, D. O. 1984, ApJ, 276, 413

Mamon, G. A., Biviano, A., & Boué, G. 2013, MNRAS, 429, 3079

Marín-Franch, A., Chueca, S., Moles, M., et al. 2012, SPIE Conf. Ser., 8450, 84503S

Martínez-Solaeche, G., González Delgado, R. M., García-Benito, R., et al. 2021, A&A, 647, A158

Martínez-Solaeche, G., González Delgado, R. M., García-Benito, R., et al. 2022, A&A, 661, A99

Mateus, A., Sodré, L., Cid Fernandes, R., et al. 2006, MNRAS, 370, 721

Mateus, A., Sodré, L., Cid Fernandes, R., & Stasińska, G. 2007, MNRAS, 374, 1457

Maturi, M., Bartelmann, M., Meneghetti, M., & Moscardini, L. 2005, A&A, 436, 37

Mazzi, A., Girardi, L., Zaggia, S., et al. 2021, MNRAS, 508, 245

McNab, K., Balogh, M. L., van der Burg, R. F. J., et al. 2021, MNRAS, 508, 157

McNamara, B. R., & Nulsen, P. E. J. 2012, New J. Phys., 14, 055023

Mercurio, A., Rosati, P., Biviano, A., et al. 2021, A&A, 656, A147

Molino, A., Costa-Duarte, M. V., Mendes de Oliveira, C., et al. 2019, A&A, 622, A178

Montero-Dorta, A. D., Chaves-Montero, J., Artale, M. C., & Favole, G. 2021, MNRAS, 508, 940

Moore, B., Katz, N., Lake, G., Dressler, A., & Oemler, A. 1996, Nature, 379, 613

Muzzin, A., Wilson, G., Yee, H. K. C., et al. 2012, ApJ, 746, 188

Nantais, J., Wilson, G., Muzzin, A., et al. 2020, MNRAS, 499, 3061

Niemiec, A., Giocoli, C., Cohen, E., et al. 2022, MNRAS, 512, 6021

Noble, A. G., Webb, T. M. A., Muzzin, A., et al. 2013, ApJ, 768, 118

Noble, A. G., Webb, T. M. A., Yee, H. K. C., et al. 2016, ApJ, 816, 48

Noeske, K. G., Weiner, B. J., Faber, S. M., et al. 2007, ApJ, 660, L43

Ocvirk, P., Pichon, C., Lançon, A., & Thiébaut, E. 2006, MNRAS, 365, 46

Oke, J. B., & Gunn, J. E. 1983, ApJ, 266, 713

Olave-Rojas, D., Cerulo, P., Demarco, R., et al. 2018, MNRAS, 479, 2328

Osterbrock, D. E. 1989, Astrophysics of Gaseous Nebulae and Active Galactic Nuclei, (University Science Books)

Osterbrock, D. E., & De Robertis, M. M. 1985, PASP, 97, 1129

Oteo, I., Sobral, D., Ivison, R. J., et al. 2015, MNRAS, 452, 2018

Pacifici, C., Kassin, S. A., Weiner, B. J., et al. 2016, ApJ, 832, 79

Pallero, D., Gómez, F. A., Padilla, N. D., et al. 2022, MNRAS, 511, 3210

Park, C., & Hwang, H. S. 2009, ApJ, 699, 1595

Peluso, G., Vulcani, B., Poggianti, B. M., et al. 2022, ApJ, 927, 130

Peng, Y.-J., Lilly, S. J., Kovač, K., et al. 2010, ApJ, 721, 193

Peng, Y.-J., Lilly, S. J., Renzini, A., & Carollo, M. 2012, ApJ, 757, 4

Peschken, N., Łokas, E. L., & Athanassoula, E. 2020, MNRAS, 493, 1375

Pharo, J., Malhotra, S., Rhoads, J. E., et al. 2020, ApJ, 888, 79

Pirzkal, N., Malhotra, S., Ryan, R. E., et al. 2017, ApJ, 846, 84

Planck Collaboration VI. 2020, A&A, 641, A6

Plat, A., Charlot, S., Bruzual, G., et al. 2019, MNRAS, 490, 978

Postman, M., Lubin, L. M., Gunn, J. E., et al. 1996, AJ, 111, 615

Puertas, S. D., Vilchez, J., Iglesias-Páramo, J., et al. 2017, A&A, 599, A71

Raj, M. A., Iodice, E., Napolitano, N. R., et al. 2019, A&A, 628, A4

Renzini, A., & Peng, Y.-J. 2015, ApJ, 801, L29

Rines, K., & Diaferio, A. 2006, AJ, 132, 1275

Roberts, I. D., Parker, L. C., Brown, T., et al. 2019, ApJ, 873, 42

Rodríguez del Pino, B., Aragón-Salamanca, A., Chies-Santos, A. L., et al. 2017, MNRAS, 467, 4200

Rozo, E., Rykoff, E. S., Bartlett, J. G., & Melin, J.-B. 2015a, MNRAS, 450, 592

Rozo, E., Rykoff, E. S., Becker, M., Reddick, R. M., & Wechsler, R. H. 2015b, MNRAS, 453, 38

Ruiz-Lara, T., Gallart, C., Monelli, M., et al. 2020, A&A, 639, L3

Sánchez, S., Avila-Reese, V., Hernandez-Toledo, H., et al. 2018, Rev. Mex. Astron. Astrofis., 54

Sánchez, S. F., Kennicutt, R. C., Gil de Paz, A., et al. 2012, A&A, 538, A8

Sánchez-Portal, M., Pintos-Castro, I., Pérez-Martínez, R., et al. 2015, A&A, 578, A30

Santini, P., Fontana, A., Castellano, M., et al. 2017, ApJ, 847, 76

Shin, K., Ly, C., Malkan, M. A., et al. 2021, MNRAS, 501, 2231

Smith, R. J., Marzke, R. O., Hornschemeier, A. E., et al. 2008, MNRAS, 386, L96

Sobral, D., Best, P. N., Smail, I., et al. 2014, MNRAS, 437, 3516

Sparre, M., Hayward, C. C., Springel, V., et al. 2015, MNRAS, 447, 3548

Speagle, J. S., Steinhardt, C. L., Capak, P. L., & Silverman, J. D. 2014, ApJS, 214, 15

Thomas, D., Maraston, C., Bender, R., & Mendes de Oliveira, C. 2005, ApJ, 621, 673

Tojeiro, R., Eardley, E., Peacock, J. A., et al. 2017, MNRAS, 470, 3720

Trager, S. C., Faber, S. M., Worthey, G., & González, J. J. 2000, AJ, 120, 165

Veilleux, S., & Osterbrock, D. E. 1987, ApJS, 63, 295

Vilella-Rojo, G., Logroño-García, R., López-Sanjuan, C., et al. 2021, A&A, 650, A68

von der Linden, A., Wild, V., Kauffmann, G., White, S. D. M., & Weinmann, S. 2010, MNRAS, 404, 1231

Wake, D. A., Bundy, K., Diamond-Stanic, A. M., et al. 2017, AJ, 154, 86

Walcher, C. J., Wisotzki, L., Bekeraité, S., et al. 2014, A&A, 569, A1

Wang, S.-C., & Yang, H. Y. K. 2022, MNRAS, 512, 5100

Wen, Z. L., Han, J. L., & Liu, F. S. 2012, ApJS, 199, 34

Wetzel, A. R., Tinker, J. L., & Conroy, C. 2012, MNRAS, 424, 232

Woo, J., Dekel, A., Faber, S. M., et al. 2013, MNRAS, 428, 3306

Woo, J., Dekel, A., Faber, S. M., & Koo, D. C. 2015, MNRAS, 448, 237

Woo, J., Carollo, C. M., Faber, S. M., Dekel, A., & Tacchella, S. 2017, MNRAS, 464, 1077

Zahid, H. J., Dima, G. I., Kewley, L. J., Erb, D. K., & Davé, R. 2012, ApJ, 757, 54

Zinger, E., Dekel, A., Kravtsov, A. V., & Nagai, D. 2018, MNRAS, 475, 3654

[1] Instituto de Astrofísica de Andalucía (CSIC), PO Box 3004, 18080 Granada, Spain
e-mail: rosa@iaa.es

[2] Departamento de Física, Universidade Federal de Santa Catarina, PO Box 476, 88040-900 Florianópolis, SC, Brazil

[3] Gemini Observatory/NSF's NOIRLab, Casilla 603, La Serena, Chile

[4] Zentrum für Astronomie, Universität Heidelberg, Philosophenweg 12, 69120 Heidelberg, Germany

[5] Institut für Theoretische Physik, Universität Heidelberg, Philosophenweg 16, 69120 Heidelberg, Germany

6 Department of Physics, University of Helsinki, Gustaf Hällströmin katu 2, 00014 Helsinki, Finland

7 Observatório do Valongo, Universidade Federal do Rio de Janeiro, 20080-090 Rio de Janeiro, RJ, Brazil

8 Instituto de Matematica Estatistica e Fisica, Universidade Federal do Rio Grande (IMEF–FURG), Rio Grande, RS, Brazil

9 Instituto de Física de Cantabria (CSIC-UC), Avda. Los Castros s/n. 39005, Santander, Spain

10 Departamento de Astronomia, Instituto de Física, Universidade Federal do Rio Grande do Sul (UFRGS), Av. Bento Gonçalves 9500, Porto Alegre, R.S, Brazil

11 Shanghai Astronomical Observatory, Chinese Academy of Sciences, 80 Nandan Rd., Shanghai 200030, PR China

12 Observatório Nacional, Ministério da Ciencia, Tecnologia, Inovação e Comunicações, Rua General José Cristino, 77, São Cristóvão 20921-400 Rio de Janeiro, Brazil

13 Department of Astronomy, University of Michigan, 311 West Hall, 1085 South University Ave., Ann Arbor, USA

14 Department of Physics and Astronomy, University of Alabama, Box 870324, Tuscaloosa, AL, USA

15 Instituto de Física, Universidade de São Paulo, Rua do Matão 1371, 05508-090 São Paulo, Brazil

16 Donostia International Physics Center (DIPC), Manuel Lardizabal Ibilbidea 4, San Sebastián, Spain

17 Centro de Estudios de Física del Cosmos de Aragón (CEFCA), Plaza San Juan 1, 44001, Teruel, Spain

18 Centro de Estudios de Física del Cosmos de Aragón (CEFCA), Unidad Asociada al CSIC, Plaza San Juan 1, 44001 Teruel, Spain

19 Ikerbasque, Basque Foundation for Science, 48013 Bilbao, Spain

20 Instituto de Física, Universidade Federal da Bahia, 40210-340 Salvador, BA, Brazil

21 Universidade de São Paulo, Instituto de Astronomia, Geofísica e Ciências Atmosféricas, R. do Matão 1226, 05508-090 São Paulo, Brazil
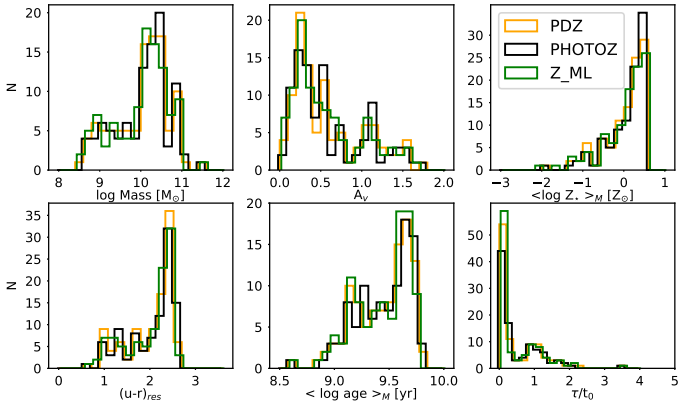
Appendix A: AMICO versions

Fig. A.1. Stellar population properties of the galaxies belonging to the cluster, using different AMICO catalogues.

As mentioned in Sect.2.2, at the moment of writing of this paper, there are three versions of the code AMICO under study. The difference among them resides in the redshift used for the computation of the amplitude, the association probability, and the rest of the parameters. One of these versions uses the best PHOTOZ (the absolute maximum of the probability density function of the redshift or zPDF) as input, however, other version uses z_{ml} (the median redshift of the zPDF) and the last one uses the zPDF itself (see Hernán-Caballero et al. 2021 for more information about the redshifts). The final version (including a group catalog for miniJPAS) will be published in a future paper (Maturi et al., in preparation). Since those results and the details about AMICO escape the scope of this work, we refer the reader to Maturi et al. (2005), Bellagamba et al. (2018a), and restrict ourselves here to the study of the stellar population properties.

The parameter we used to select our set of galaxies is the association probability. When changing the redshift, the association probability is affected as well. As a consequence, some galaxies may be considered members or not of the cluster. In fact, the total number of galaxies changes (99 galxies using the PHOTOZ, 95 using the z_{ml} and 114 using the zPDF. Not only does the number of galaxies change, but also the set of the common galaxies between two different versions of the code does not equal the smallest set of the two, although they are very similar overall. There are 84 galaxies in common among the three sets, and the larger discrepancies are 12 galaxies that appear with PHOTOZ and zPDF but not with z_{ml}, and other 12 galaxies that only appear with zPDF .

In Fig. A.1, we show the distribution of the stellar properties obtained with the three different versions. These distributions are practically the same, and the differences that appear are mainly due to the different number of galaxies in each set, but the whole image of the cluster remains the same. This is an important result for us, since our results remain valid independently of the final version that may be chosen, as well as for AMICO, since it proves that the cluster catalogue is robust regardless of the redshift definition being used.

Appendix B: Comparison of J-PAS data with GMOS spectroscopy.

We carried out a spectroscopic follow up of the cluster with the Gemini Multi Object Spectrometers (GMOS Hook et al. 2004) mounted on the Gemini North telescope (Gemini program ID: GN-2020A-DD-203, PI: Carrasco). In total, we measured the spectroscopic redshifts for 53 galaxies observed with GMOS, of which 38 galaxies are members of the cluster. Figure B.1 shows a comparison among the J-spectra and the spectra obtained from GMOS for two galaxies belonging to the cluster. This comparison shows the power of J-PAS photometric system to provide information equivalent to the spectroscopy data. We have already shown that J-spectra can retrieve the stellar population properties with similar precision to spectroscopic datasets with S/N≥10 (González Delgado et al. 2021). With respect to GMOS data, J-spectra have a better S/N and it covers a larger wavelength range that is not affected by calibration issues at the wavelengths limits. Furthermore, many of the GMOS spectra do not cover Hα wavelength range; and it is in only seven of these galaxies that Hα is observed. The right panel of Fig. B.1 shows an example of a galaxy with measured Hα emission through the ANN, and clearly detected in the J-spectra, that is not covered in the GMOS spectrum. In addition, miniJPAS data allowed us to observe most of the galaxies of the cluster brighter than 22.5 magnitude in the r_{SDSS} band. In contrast, MOS spectroscopy is limited by the minimum distance between fibers, which prevent the simultaneous observations of galaxies that are close in the sky, and some fibers are contaminated by several close objects. Thus, J-PAS data is more suitable than GMOS spectra for our analysis.

In addition to the galaxies in the clusters, our GMOS observations include more galaxies of miniJPAS. To test our ELG detection methods, we included all the galaxies from miniJPAS that were observed in the $H\alpha$ wavelength range. This includes seven spectra of the galaxies belonging to the cluster plus another six galaxies outside the cluster that show Hα emission in their GMOS spectra. Table B.1 summarises the results obtained with both methods for these galaxies. We note that none of the methods classify as ELG any of the galaxies that show no Hα emission in their spectra (covering the corresponding wavelength). The different criteria for red and blue galaxies is shown to be required in this table. If we choose the same $\sigma = 1$ detection level for blue or red galaxies, we find that red galaxies that actually show no emission line are classified as ELG. If we choose the same $\sigma = 3$ detection level, we end up selecting too few blue ELG which do in fact show Hα emission (seen in the GMOS spectra). This is a consequence of the different brightness of red and blue galaxies: the mean and standard deviation values of the r_{SDSS} magnitudes is 20.37 ± 0.82 mag for red galaxies and 21.58 ± 0.89 mag for blue galaxies. This also produces the difference between the S/N ratios at the Hα wavelength range for the red and blue galaxies. The median value of the S/N of the three filters closer to Hα at the cluster redshift is 14.67 for red galaxies and 5.27 for blue galaxies, which is almost three times better for red galaxies than for blue galaxies.
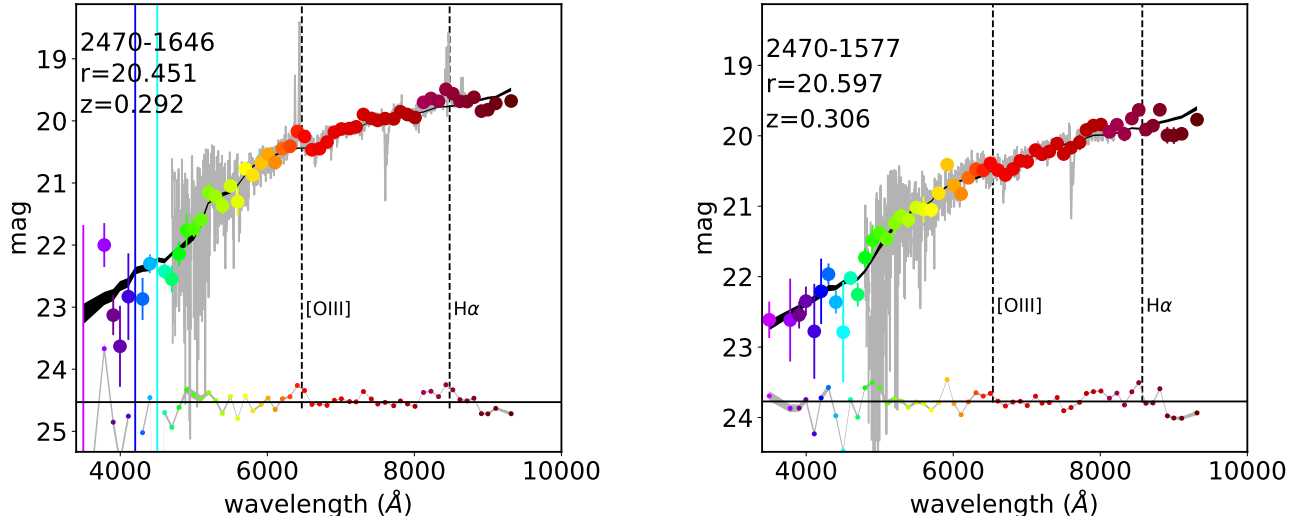
Fig. B.1. Comparison among the J-spectra and the GMOS spectra of two galaxies belonging to the cluster. Colour points represent the J-spectra. Grey lines represent the GMOS spectra. The black band shows the magnitudes of the mean model ± one σ uncertainty level. The difference between the model and the mean model fitted magnitudes are plotted as a small coloured points around the black bottom line. Vertical, black dashed lines show the wavelengths corresponding to [OIII] and Hα emission lines.

Table B.1. Results of the emission line classification method

Galaxies with Hα emission in GMOS	Median error classification	ANN classification	Median error notes	ANN notes
2470-1168	Yes	Yes	-	-
2470-494	Yes	Yes	-	-
2470-536	?	?	J-spectra shows no emission	Unable to calculate values
2470-1646	Yes	Yes	-	-
2470-1744	No	No	Classified as line-emission when using the spectroscopic redshift	EW$_{min}$=35.31, EW=2.44±6.32
2470-2129	Yes	Yes	-	-
2470-2328	Yes	Yes	-	-
2470-2524	Yes	Yes	-	-
2470-2401	Yes	Yes	-	-
2470-2667	?	?	J-spectra shows no emission	Unable to calculate values
2470-1920	Yes	Yes	-	-
2470-1625	Yes	Yes	-	-
2470-2403	Yes	Yes	-	-

Notes. First column shows the J-PAS ID of the galaxies with Hα emission in GMOS. Second and third columns show if the galaxy was classified as an emission line one with the median error method and the ANN method, respectively. Fourth and fifth columns show some comments on why each method failed to classify the galaxy properly.

Appendix C: ELG classification

In Sect. 4.3, we describe how we classified the ELG into SF galaxies and AGNs using the WHAN and BPT diagrams, and we explain that it is difficult to uniquely classify each galaxy. Figure C.1 illustrates this difficulty and the uncertainty that we face in this classification.

Figure C.1 shows two galaxies that are classified as SF in the WHAN diagram and as Seyfert galaxies in the BPT. The J-spectra of the galaxy 2470–3670 shows that it is probably an extreme emission line galaxy (EELG, see Iglesias-Páramo et al. 2022), due to its weak continuum and its strong emission lines. However, its Seyfert classification is poorly constrained by the [NII]/Hα ratio and error. However, its probability of being a SF galaxy in the WHAN diagram is equal to 1, and so, this galaxy is classified as SF. On the contrary, 2470–1646 is classified as well-constrained in the BPT as a Seyfert. In addition, its GMOS spectrum shows [OIII]/Hβ and [NII] /Hα ratios of Seyfert galaxies. In the WHAN diagram, the J-spectra data place it close to the SF region, and the probability of being classified as a SF is 0.55. A deep inspection of the J-spectra images at the Hα and close continuum filters shows that it is a spiral galaxy with extended Hα emission that could be produced by the AGN and young stars. This galaxy is finally classified as an AGN, although it has SF properties.

These cases motivate our simpler classification according with their probability in the WHAN diagram as SF or BPT diagram as AGN. Other cases that are between the 'composite' regions in the WHAN or BPT are classified as SF-AGN. Table C.1 shows the position on each diagram for every galaxy and the final classification given to it, attending to the criteria described in Sect. 4.3.

Table C.1. Classification of the ELG population attending to the WHAN and BPT diagrams.

ID	WHAN	BPT	Final classification
2470-1030	SF-Seyfert	Seyfert	AGN
2470-1117	SF	SF-Seyfert	SF
2470-1168	SF	SF	SF
2470-1174	SF	SF-Seyfert	SF
2470-1205	SF-Seyfert	Seyfert	AGN
2470-1287	SF	SF-Seyfert	SF
2470-1344	SF	SF	SF
2470-1376	SF	SF-Seyfert	SF
2470-1401	SF	SF	SF
2470-1457	SF	SF	SF
2470-1478	SF-Seyfert	SF-Seyfert	SF-AGN?
2470-1506	SF	SF	SF
2470-1587	SF-Seyfert	Seyfert	AGN
2470-1593	SF-LINER	Seyfert	AGN
2470-1646	SF	Seyfert	AGN
2470-1650	SF	SF-Seyfert	SF
2470-1695	LINER	SF-LINER	AGN
2470-1757	SF	SF-Seyfert	SF
2470-1771	LINER	LINER	AGN
2470-1789	SF	SF	SF
2470-1827	SF	SF	SF
2470-1941	SF	SF	SF
2470-2129	SF	SF-Seyfert	SF
2470-2328	SF	SF-Seyfert	SF
2470-2350	SF	SF	SF
2470-2446	SF	SF	SF
2470-2493	SF	SF	SF
2470-2524	SF	SF	SF
2470-2693	SF-Seyfert	SF-LINER	SF-AGN?
2470-2791	SF	SF	SF
2470-2799	SF	SF	SF
2470-2832	SF-LINER	Seyfert	AGN
2470-2910	SF	SF-Seyfert	SF
2470-2949	SF	SF	SF
2470-2964	SF-LINER	Seyfert	AGN
2470-3255	SF-Seyfert	SF-LINER	SF-AGN?
2470-3345	SF	SF	SF
2470-3670	SF	Seyfert	SF
2470-3712	SF-Seyfert	Seyfert	AGN
2470-3848	SF-Seyfert	SF-Seyfert	SF-AGN?
2470-4414	SF	SF	SF
2470-4691	SF-Seyfert	Seyfert	AGN
2470-492	SF	SF	SF
2470-494	SF	SF	SF
2470-5523	SF	SF	SF
2470-587	SF	SF	SF
2470-701	SF	SF	SF
2470-734	SF-Seyfert	SF-LINER	SF-AGN?
2470-823	SF-Seyfert	Seyfert	AGN

Notes. First column shows the ID of the galaxy. Second and third columns show the classification on the WHAN and BPT diagrams, respectively. Fourth column shows our final consideration using both diagrams and taking into account the errors of the predictions. Question marks indicate the possibility of the galaxy belonging to such category, but express our insecurity due to errors being to big, the spectrum being too noisy or to a great discrepancy in the WHAN and BPT classes.
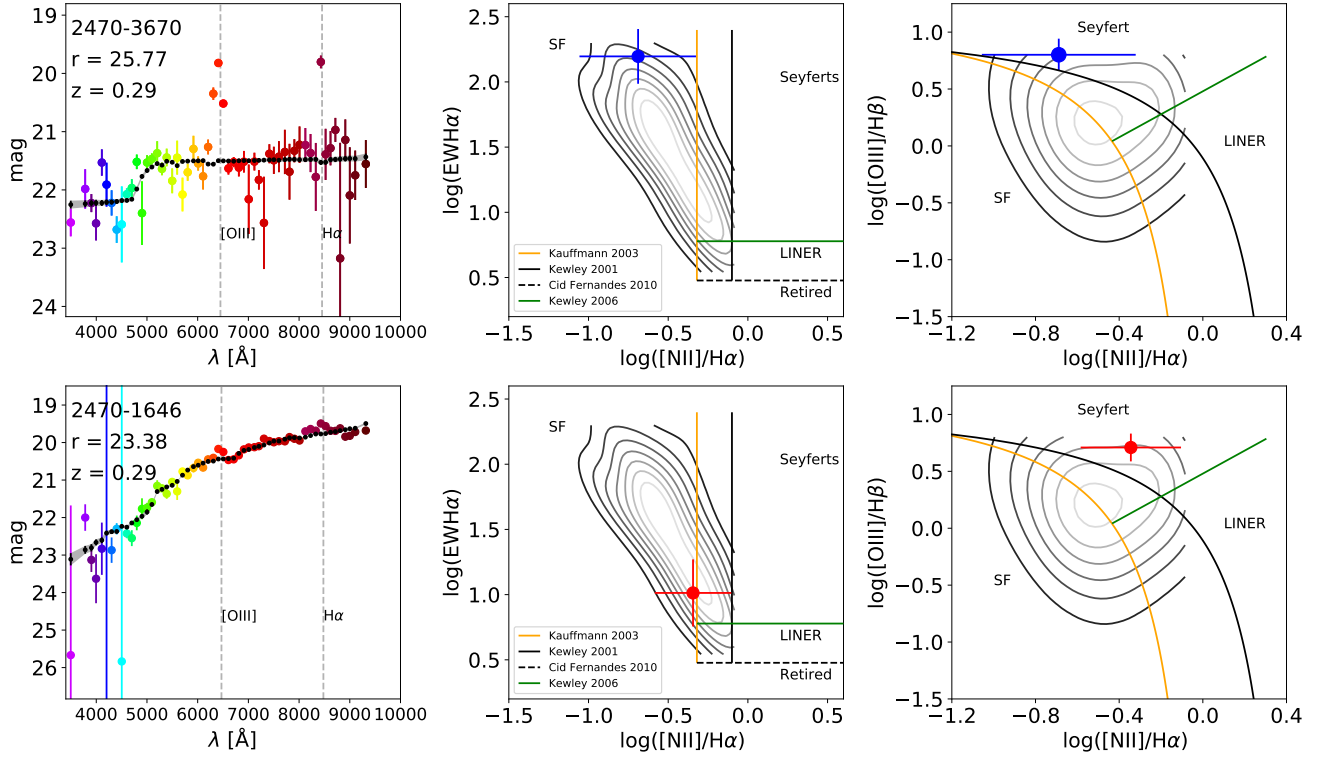
Fig. C.1. Example of a star-forming galaxy (top row) and a Seyfert galaxy (bottom row). From left to right, the panels in each galaxy show the spectra and its position in the WHAN and BPT diagrams (where the contours represent this work's galaxy density in each diagram). The solid orange and black lines represent the Cid Fernandes et al. (2010) transposition of the Kauffmann et al. (2003a) and Kewley et al. (2001) SF-AGN distiction criteria, and the green solid line represents the transposition of the Kewley et al. (2006) made by Cid Fernandes et al. (2010). The dashed black line represents the distinction between retired galaxies and LINERs (Cid Fernandes et al. 2011).